### Title
Representation of Atmospheric Water Budget and Uncertainty Quantification of Future Changes in CMIP6 for the Seven U.S. National Climate Assessment Regions




### Journal
Journal of Climate, 35(22)

### ISSN
0894-8755



### Authors
Sengupta, Agniv
Waliser, Duane E
Massoud, Elias C
et al.



### Publication Date
2022-11-15

### DOI
10.1175/jcli-d-22-0114.1

# Representation of Atmospheric Water Budget and Uncertainty Quantification of Future Changes in CMIP6 for the Seven U.S. National Climate Assessment Regions

Agniv Sengupta,[a,b] Duane E. Waliser,[b,d] Elias C. Massoud,[c] Bin Guan,[b,d] Colin Raymond,[b] Huikyo Lee[b]

[a] *Center for Western Weather and Water Extremes, Scripps Institution of Oceanography, University of California, San Diego, La Jolla, California*

[b] *Jet Propulsion Laboratory, California Institute of Technology, Pasadena, California*

[c] *University of California, Berkeley, Berkeley, California*

[d] *Joint Institute for Regional Earth System Science and Engineering, University of California, Los Angeles, Los Angeles, California*

*Corresponding author*: Agniv Sengupta, agsengupta@ucsd.edu

ABSTRACT

Observation-based climate model evaluation and future projections help policymakers in developing action plans for efficient management of water resources and mitigation of the impacts of hazardous extremes. Apart from this socioeconomic importance, the scientific value cannot be overstated, especially in light of the upcoming Fifth U.S. National Climate Assessment (NCA) report. In this study, we evaluate the realism of hydroclimate variability in the historical simulations of a suite of coupled general circulation models (CGCMs) participating in the Sixth and Fifth phases of the Coupled Model Intercomparison Project (CMIP6 and CMIP5). Our results demonstrate systematic biases in the simulated seasonal precipitation – most prominently, wet bias over the mountainous West in winter, and dry bias over the Central Plains in summer. A distinctive feature of this work is our focus on the examination of the atmospheric water budget, in particular, the relative importance of remote and local contributions – convergence of moisture fluxes and local land surface processes (evapotranspiration) respectively – in helping produce precipitation. This diagnosis reveals that the leading contribution of the remote influence in winter is overestimated by the CMIP6 multi-model mean (MMM), whereas the local influence which is more influential in summer is underestimated. Our results aid in understanding the drivers of seasonal precipitation over the U.S., where precipitation will likely increase by the end of the century but with significant model disagreement for the summer and fall. In support of ongoing NCA efforts, our study aims to contribute a comprehensive, regional-level analysis of the moisture budget and emphasizes the importance of realistically simulating its major components in CGCMs.

## 1. Introduction

Changes to the water cycle in a warming world can have profound impacts on humanity and the environment because its atmospheric and terrestrial components are integral to life on land and influence circulation in the atmosphere and the oceans. These changes especially those exceeding the threshold of natural variability are of great scientific interest (Easterling et al. 2017; USGCRP 2017). They include, but are not limited to, variations in precipitation, evapotranspiration, atmospheric humidity, and horizontal moisture flux (Bosilovich et al. 2005; Held and Soden 2006; Huntington 2006; Rodell et al. 2015). Due to the heterogeneity in the distribution of climate controls over the planet, these changes, however, are not uniform and have distinct regional patterns. It is this regional manifestation that determines the distribution of sustainable water supply, and the potential for operational management of water resources, including planning for and responding to, prevention of extreme episodes. Therefore, a clear understanding of the hydroclimatic controls of current and future climate on the regional scale is of fundamental societal and scientific importance.

At a global level, projections of future change in our climate system are provided by the Intergovernmental Panel on Climate Change (IPCC) through its Assessment Reports (ARs). For instance, Collins et al. (2013) presents the long-term projections for the end of the 21st century based on global climate models participating in the Coupled Model Intercomparison Project Phase 5 (CMIP5) under various Representative Concentration Pathways (RCP) scenarios. Meanwhile, national assessments of future climatic changes under multiple scenarios of increasing greenhouse gas concentrations have been conducted in the United States [through its National Climate Assessment (NCA), the most recent one being the Fourth NCA (NCA4; USGCRP 2017) Report], United Kingdom (Murphy et al. 2018), Australia (CSIRO and Bureau of Meteorology, 2015), India (Krishnan et al. 2020), and others. The fundamental basis of these climate assessments are fully-coupled Earth-system models driven by potential future emissions and socioeconomic-development scenarios. For further scientific understanding, and to devise and evaluate potential mitigation and adaptation strategies, it is essential to closely examine the fidelity of these global coupled climate models in representing important Earth system processes and related feedbacks.

The water cycle through its fluxes and reservoirs forms an integral component of the Earth system, as well as a critical enabler of human activities whose historical characteristics are threatened by climate change (Tabari et al. 2021). Several global water cycle analyses have been conducted starting with the earliest analyses (Nace 1969; Korzoun 1974) which relied on limited observations to estimate globally averaged fluxes of precipitation and evapotranspiration. More comprehensive water cycle assessments have been conducted in the recent decades (e.g., Chahine 1992; Oki et al. 1999; Oki and Kanae 2006; Trenberth et al. 2007; Waliser et al. 2007; Rodell et al. 2015), which, through rigorous accounting of errors, reveals the extent to which the water budget can be closed over multiple regions with the present observational resources; besides this, these notable global assessments provide a benchmark for Earth system model evaluations.

With the goal of informing the upcoming Fifth NCA (NCA5) report, the present study focuses on the atmospheric water budget and the realism of associated simulations by coupled models participating in the most recent phase (phase 6) of the CMIP project (CMIP6;

Eyring et al., 2016). The domain of the study is the continental United States (CONUS) — a region that includes a variety of hydroclimatic regimes and is densely observed, providing avenues for comprehensive model assessment. It comprises of seven NCA regions — Northwest, Southwest, Northern Great Plains, Southern Great Plains. Midwest, Northeast, and Southeast; all outlined in Fig. 1. Across the U.S., the annual precipitation has increased by 5% over the 1901–2012 period as reported in the Third National Climate Assessment (NCA3; Walsh et al. 2014) report, with the more recent NCA4 reporting an increase of 4% over the 1901–2015 period. These changes are far from uniform and have important regional and seasonal differences; the Northeast, Midwest, and Great Plains have experienced increases, while parts of the Southwest and Southeast have had decreases in precipitation (Easterling et al. 2017).

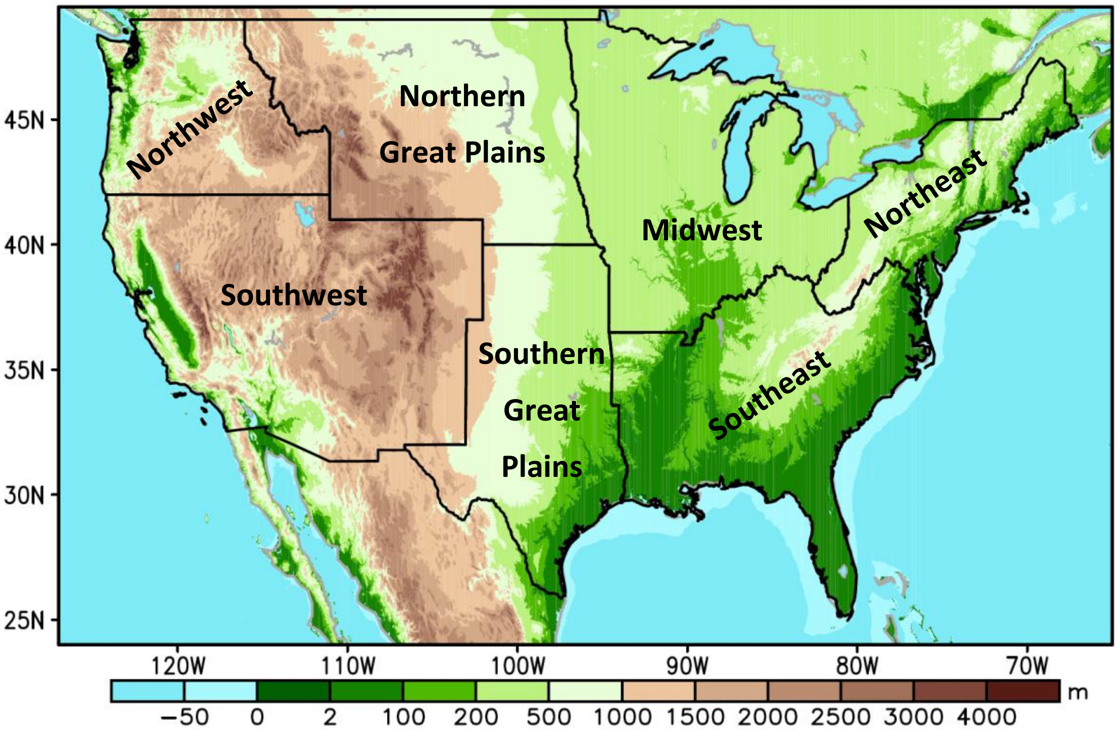


Fig. 1. The elevation map of the study region encompassing the seven National Climate Assessment (NCA) regions of the CONUS – Northwest, Southwest, Northern Great Plains, Southern Great Plains, Midwest, Northeast, Southeast. Brown/green shading denotes elevation (in meters), and blue shading denotes bathymetry. Topography data is obtained from NOAA'S National Oceanographic Data Center's ETOPO1 Global Relief Model (Amante and Eakins 2009), a 1 arc-min resolution relief model of the Earth's surface developed from diverse global and regional digital datasets and then shifted to a common horizontal and vertical datum.

Focusing over North America, hydroclimate variability has been extensively studied from both observational and modeling analyses, including a number of studies for the Great Plains of the central U.S. during the warm season (e.g., Trenberth and Guillemot 1996; Barlow et al. 2001; Schubert et al. 2004; Ruiz-Barradas and Nigam 2005, 2006; Feng et al. 2016), and for the western U.S. (Guan et al. 2010; Dettinger et al. 2011; Baker and Huang 2012, 2014; Gershunov et al. 2017; Massoud et al. 2020a; McKinnon and Deser 2021). In this context, Cook and Seager (2013) noted a shift in the seasonality of the North American Monsoon to late summer under global warming. More recently, Massoud et al. (2020b) documented the CMIP5 end-of-the-century projections of precipitation over CONUS by constraining the spread of model uncertainty using Bayesian model averaging. Watterson et al. (2021) analyzed the atmospheric moisture budget in CMIP6 models and discussed implications for future projections of mean and heavy rainfall; however, only ten models were analyzed for a specific experiment — the idealized rising-CO2 (1pcCO2), and no other CMIP6 forcing scenarios. With the above studies in mind, the present study is novel in the level of detail it provides in regard to diagnosing the components of the atmospheric water budget for each individual U.S. NCA region and evaluating the fidelity of the state-of-the-art simulations from a much larger suite of CMIP6 and CMIP5 coupled climate models. Specifically, this investigation seeks to unravel the relative contributions of atmospheric water budget terms — local and remote influences (evaporation and moisture fluxes, respectively) — in generating precipitation over individual NCA regions.

The CONUS lies between the high-latitude regions, which are projected to become wetter, and the subtropical zone, which is projected to become drier (Collins et al. 2013). As such, there exists considerable uncertainty in the future projected changes in precipitation, in particular for the midlatitude regions. On the other hand, evaporation rates have already increased by 10% globally in recent decades (Pascolini-Campbell et al. 2021) and are projected to increase in a warmer world with major impacts on the hydrological cycle (Kundzewicz 2008; IPCC 2013). As a result of increasing evaporation coupled with higher atmospheric water vapor, the frequency and intensity of landfalling atmospheric rivers, which are influential on a suite of hydrometeorological extremes, are projected to increase for the U.S. West Coast (e.g., Gao et al. 2015; Warner et al. 2015; Espinoza et al. 2018). On the other hand, mesoscale convective systems — the primary mechanism of warm-season precipitation in the central U.S. — are projected to increase in frequency and intensity (medium model confidence) (Easterling et al. 2017; USGCRP 2017). NCA4 also reported a projected increase in the intensity (with medium model confidence) and frequency (with low confidence) of hurricanes in the North Atlantic. Thus, there exist significant uncertainties in the future projections, especially over regions where changes of the opposite sign are projected across models. Sources of such uncertainties include inadequacies in model formulations, future emission scenarios, the extent of human influence, technological advancements, social/government actions. With simulations and projections now available from the latest CMIP6 archive, understanding how models represent the various components of the water cycle presents an opportunity for tracking progress across the CMIP phases of experiments and refining related regional hydroclimate projections.

The present study is motivated by the lack of comprehensive NCA-focused analyses using a moisture-budget framework. Section 2 discusses the observational and reanalysis datasets, CMIP6 and CMIP5 model simulations and projections, and analysis methods. The representation of the atmospheric water budget components in the historical climate simulations over the U.S. NCA regions is critiqued in section 3, including an evaluation of the models' skill in replicating the annual mean and annual cycle of observed precipitation. This approach facilitates the diagnosis of systematic model biases and tracks improvements made across the latest two phases of CMIP experiments. The relative contributions from moisture flux convergence (remote) and evaporation (local) to precipitation variability are also compared in this section. The uncertainties in model simulations of precipitation and evaporation are presented in section 4, while projected future changes for the end of the 21$^{st}$ century and associated uncertainty are described in section 5. Concluding remarks, including implications of this analysis for the upcoming NCA5 report, follow in section 6.

## 2. Datasets and analysis method

The spatial domain of this investigation involves the continental United States, while the temporal scale focuses on the mean monthly to mean annual hydroclimate during the three decades (1981–2010) of historical coupled climate simulations, and end-of-century (2071–2100) projections of future climate.

### *a. Historical Climate Simulations and Future Projections*

The historical simulations of the twentieth-century climate are evaluated in this study, where GCMs are forced by greenhouse gas emissions, volcanic and anthropogenic aerosol loadings, and solar irradiance. The pertinent features of the coupled models from the major climate research centers of the world, as part of World Climate Research Programme (WCRP)'s CMIP6 and CMIP5, assessed in this study (32 CMIP6 and 20 CMIP5 CGCMs) are noted in Table 1 and Table S1 (of the supplemental material) respectively. To assess the future change and associated uncertainty, we analyze the projections from the Shared Socioeconomic Pathway (SSP)5-8.5 in the CMIP6 archive (O'Neill et al. 2016). The SSP5-8.5 scenario is an update of the CMIP5 version of the representative concentration pathway 8.5 (RCP8.5); it lies at the higher end of future pathways and assumes that greenhouse gas emissions are high enough to reach a radiative forcing of 8.5 W $m^{-2}$ in 2100. The atmospheric water budget components analyzed here involve precipitation, evapotranspiration, vertically integrated horizontal moisture transport, and water vapor path, in addition to the atmospheric circulation. The multi-model mean (MMM) of the ensemble of models (for their first run, i.e., "r1" member) is used for deriving the climatological mean. Analysis of the MMM is performed by interpolating the individual model fields onto a common spatial resolution, identical to that of the given baseline observation, or reanalysis dataset.

The historical model simulations generally start in the second half of the 1800s and end in the mid-2010s, while the future projections usually extend out to at least the end of the 21$^{st}$ century. The period of evaluation here will focus on the recent three full decades of available data (1981–2010) to determine the realism of the present-day climate simulations compared to the observations. The future change computed here refers to the change of the projected climatological mean for the end-of-century (2071–2100) period relative to that simulated for their corresponding historical (1981–2010) period.

| **Modeling Institution (Country)** | **CMIP6 model name** | **Resolution (lon x lat)** |
|---|---|---|
| Australian Community Climate and Earth System Simulator (Australia) | ACCESS-CM2 | 192x144 |
| | ACCESS-ESM1-5 | 192x145 |
| Beijing Climate Center (China) | BCC-CSM2-MR | 320x160 |
| | BCC-ESM1 | 128x64 |
| Canadian Centre for Climate Modelling and Analysis (Canada) | CanESM5 | 128x64 |
| Chinese Academy of Science (China) | CAS-ESM2-0 | 256x128 |
| National Center for Atmospheric Research (USA) | CESM2 | 288x192 |

| | | |
|---|---|---|
| | CESM2-FV2 | 144x96 |
| | CESM2-WACCM | 288x192 |
| | CESM2-WACCM-FV2 | 144x96 |
| Energy Exascale Earth System Model (E3SM) Project (USA) | E3SM-1-0 | 360x180 |
| | E3SM-1-1 | 360x180 |
| | E3SM-1-1-ECA | 360x180 |
| Chinese Academy of Science (China) | FGOALS-g3 | 180x80 |
| Geophysical Fluid Dynamics Laboratory (USA) | GFDL-ESM4 | 288x180 |
| NASA Goddard Institute for Space Studies (USA) | GISS-E2-1-G | 144x90 |
| | GISS-E2-1-G-CC | 144x90 |
| | GISS-E2-1-H | 144x90 |
| Institute for Numerical Mathematics (Russia) | INM-CM5-0 | 180x120 |
| Institut Pierre Simon Laplace (France) | IPSL-CM6A-LR | 144x143 |
| National Institute of Meteorological Sciences, Korea Meteorological Administration (Korea) | KACE-1-0-G | 192x144 |
| Manabe Climate Model, University of Arizona (USA) | MCM-UA-1-0 | 96x80 |
| Japan Agency for Marine-Earth Science and Technology/ Atmosphere and Ocean Research Institute, the University of Tokyo (Japan) | MIROC6 | 256x128 |
| Max Planck Institute (Germany) | MPI-ESM-1-2-HAM | 192x96 |
| | MPI-ESM1-2-HR | 384x192 |
| | MPI-ESM1-2-LR | 192x96 |
| Meteorological Research Institute (Japan) | MRI-ESM2-0 | 320x160 |
| Nanjing University of Information Science and Technology (China) | NESM3 | 192x96 |

| | | |
|---|---|---|
| Norwegian Climate Center (Norway) | NorCPM1 | 144x96 |
| | NorESM2-LM | 144x96 |
| Seoul National University (Korea) | SAM0-UNICON | 288x192 |
| Research Center for Environmental Changes, Academia Sinica (Taiwan) | TaiESM1 | 288x192 |

Table 1. Description of CMIP6 models used in the present study.

*b. Observed Precipitation*

The baseline evaluation utilizes four different gridded precipitation datasets for the observed seasonal and regional distribution of precipitation, including its annual cycle, and associated uncertainty estimates. Compared to individual station-based data, gridded in situ products are usually preferred for model evaluation as it represents the precipitation averaged over a grid cell thereby facilitating comparison against corresponding climate model simulation (Zhang et al. 2011, Gibson et al. 2019). In situ products draw from rain gauge networks employing different interpolation schemes, elevation corrections, and other gridding and processing methods.

The National Oceanic and Atmospheric Administration (NOAA) Climate Prediction Center (CPC)'s Unified CONUS dataset (CPC Unified; Xie et al. 2007, Chen et al. 2008) is a gridded precipitation product available at 0.25° by 0.25° resolution over the domain 20°N–49.5°N, 233.75°E–292.75°E for the period January 1948–present. The project was developed with the goal of unifying the suite of available precipitation products at CPC, including station data from the U.S. rain gauge network, over the land while taking advantage of the optimal interpolation algorithm. The second precipitation dataset used is the Oregon State University Parameter-Elevation Regressions on Independent Slopes Model (PRISM; Daly et al. 2008), available at a 4-km spatial resolution. It draws station data from the Cooperative Observer Program (COOP) and Snowpack Telemetry (SNOTEL) networks and uses linear precipitation–elevation correction scheme that applies weights based on elevation. Third, the German Meteorological Service's (DWD) Global Precipitation Climatology Centre Full Data Product (GPCC; Schneider et al. 2018) on a 0.25° continental grid is used in this study. It is a quality-controlled, global land-surface precipitation dataset for the January 1891–December 2016 period, derived from ~85,000 stations worldwide featuring record durations of 10 years or more. Last, the analysis draws from the Climatic Research Unit

Time-Series Version 4.02 (CRU-TS4.02; Harris et al. 2020) available at 0.5° by 0.5° resolution. It is a high-resolution, global, gridded data of month-by-month variation in climate over the land points for the January 1901−December 2017 period.

To assess the uncertainty in the observational datasets, we computed the climatological means, both annually and seasonally, by taking area averages over each of the seven NCA regions; all documented in Table S2 (of the supplemental material). This dataset intercomparison reveals that the inter-product deviations are modest in the observed record, within 5% of the climatological means. This leads to our preference for the CPC Unified product for the assessment of historical model simulations, given its CONUS-centric focus and spatial resolution ensuring computational efficiency.

*c. ERA5 Reanalysis*

The fifth generation of the European Centre for Medium Range Weather Forecasting's (ECMWF) Reanalysis (ERA5; Hersbach et al., 2020), a state-of-the-art global reanalysis product obtained from a 4-dimensional variational (4D-Var) data assimilation system, is used for the diagnosis of atmospheric water budget constituents and to characterize the circulation associated with the seasonal precipitation. This global reanalysis generated via assimilation of historical observations (satellite and in situ) is available at a monthly resolution on a 0.25° by 0.25° grid from the year 1979–present. While reanalyses in the past have had deficiencies in their water budget (Berrisford et al., 2011), ERA5 has an improved global hydrological budget compared to ERA-Interim (Hersbach et al. 2020, their Fig. 23). This leads us to our choice of ERA5 as the target dataset for comparative assessment of evapotranspiration, zonal and meridional winds, total column water vapor, vertical integrals of horizontal moisture fluxes, and their divergences against corresponding fields from CMIP6.

*d. Analysis Method*

In this study, the comparative significance of the components of the vertically integrated moisture conservation equation is analyzed; the atmospheric moisture budget which can be written as (e.g., Watterson et al. 2020): $P = E + MFC - \frac{\partial W}{\partial t}$, (1)

where P is precipitation, E is evaporation from the surface, $MFC = -\nabla . F$ is the convergence of vertically integrated horizontal water vapor flux, and W is the total column water vapor or precipitable water. Also, $\frac{\partial}{\partial t}$ is the local rate of change, $\nabla$ is the gradient operator. Meanwhile, $F = \frac{1}{g}\int_0^{p_s} q\, V_h\, dp$, and, $W = \frac{1}{g}\int_0^{p_s} q\, dp$, where $q$ is specific humidity, $g$ is gravity, $p_s$ is the pressure at the Earth's surface, and $V_h$ is the horizontal wind vector. Here, we estimate the contributions from the right-hand terms of Equation (1) towards precipitation variability for each U.S. NCA region.

A common approach in regional hydroclimate studies focusing on future changes is to consider the GHG-induced "thermodynamic influence" of increased atmospheric water vapor in a warmer world. However, this GHG-induced thermodynamic effect, which potentially increases precipitation, also stabilizes the atmosphere via top-heavy heating, thereby reducing convection mass flux and, ultimately, precipitation. In other words, the two effects of the thermodynamic influence tend to offset each other (Vecchi and Soden 2007; Chadwick et al. 2016; Jin et al. 2020). As demonstrated in Wang et al. (2020), the GHG radiative forcing generates non-uniform warming, which may drive changes in atmospheric circulation that ultimately determines the likely future regional precipitation change. Therefore, in our present analysis of future projected precipitation changes (Section 5), we include a focus on the "dynamic influence" of changes in atmospheric circulation. In other words, our discussion of the future precipitation changes provides supporting evidence from likely changes in atmospheric circulation.

## 3. Atmospheric water budget in historical climate simulations

### *a. Precipitation*

#### 1) Simulation of Seasonal Precipitation and Circulation

The twentieth-century (i.e., historical) simulations of climate provide unique avenues for evaluation of models whose projections of future climate will form the foundation of the most recent IPCC report, the IPCC-AR6. The spatial distribution of precipitation and associated 850-hPa winds in observations/reanalysis and the bias in the corresponding CMIP6 and CMIP5 multi-model ensemble is displayed at seasonal resolution in Fig. 2. The observed winter mean precipitation is characterized by the maximum over the northwestern and western U.S. with notably large magnitude (~ 4.2 mm day$^{-1}$) in coastal Washington, Oregon, and northern California. On the other hand, the Southeast experiences similar precipitation year-round with a weak spring maximum (~ 3.6–3.9 mm day$^{-1}$). The warm-season (summer) months of June–August exhibits a peak (~ 3.3–3.6 mm day$^{-1}$) over the central United States

(35°–45°N, 100°–90°W) and an even wetter one (~ 4.2 mm day$^{-1}$) along the southeastern coast. Also evident in Fig. 2 are regions of fall season precipitation focused primarily along the Gulf coast states (aggregating ~ 3.3–3.6 mm day$^{-1}$). A salient feature of the seasonal circulation is the primarily zonal flow in the mid-latitudes over the northern states. Interestingly, the warm season months of June–August – the wettest part of the year for the Great Plains – sees the advent of onshore southerly winds (~ 4–5 m s$^{-1}$) from the Gulf of Mexico, which also helps to explain the climatological aridity gradient around 100°W (Seager et al. 2018). The historical climate simulations of both the CMIP6- and the CMIP5 models demonstrate significant large-scale biases: wet biases over the leeward side of the mountainous regions of the West (e.g., the Cascades and the Sierra) in winter, and dry biases in the Gulf Coast states with extension into the Great Plains in summer. The dipole structure of the bias in the Pacific Northwest and the Sierra Nevada, notably in the climatological wet season (winter), suggests a lack of model resolution of orography in this region. The other notable deficiency – an expansive summer precipitation deficit (~ 0.6–0.9 mm day$^{-1}$) in the Great Plains – may result from an underestimation of remote and local contributions to precipitation. The simulated 850-hPa circulation reveals northeasterly/northerly wind biases (~ 2–3 m s$^{-1}$) over the Southeast in the CMIP5 MMM across all seasons. This acts to weaken the prevailing southerly/southwesterly flow that transports moisture from the Gulf of Mexico. These wind biases are much weaker (~ 1 m s$^{-1}$) in the CMIP6 MMM, which indicates an improvement in the representation of the regional atmospheric circulation. The precipitation bias is, however, almost unchanged between CMIP5 and CMIP6, which prompts an investigation into the model representation of local contributions to the precipitation in the Southeast (see Section 3e).

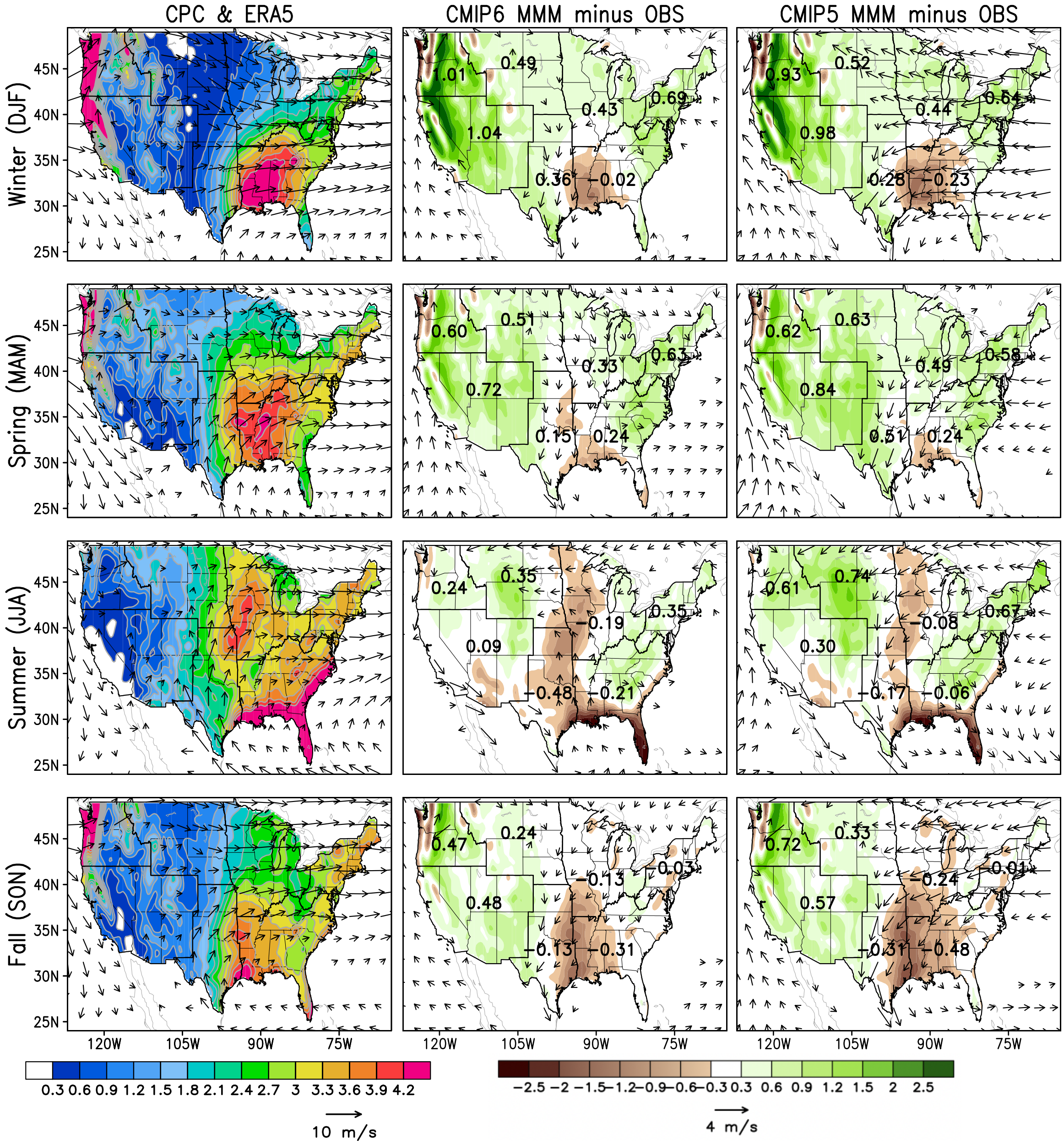


Fig. 2. Seasonal mean precipitation (mm day$^{-1}$; from NOAA CPC-Unified) and 850-hPa winds (m s$^{-1}$; from ERA5 Reanalysis) in observations/reanalysis (first column), and CMIP6 and CMIP5 differences, i.e., their respective multi-model ensemble mean (MMM) minus observations (second and third columns). The period of analysis is 1981–2010 for observations and the CMIP6 models, and 1981–2004 for CMIP5. The number in bold in the second and third columns represent the area-averaged precipitation bias values over the seven NCA regions.

## 2) Simulation of Precipitation Annual-Mean

The individual models' skill in simulating the mean annual precipitation, obtained as biases from the observed climatological precipitation in 32 historical simulations, is assessed in Fig. 3; the CPC-Unified (Fig. 3i) is the validation target for these simulations. These models display a varying degree of fidelity with some systematic regional biases evident across a majority of them. Focusing on the southeastern United States, specifically the Gulf Coast, and extending into the central Plains, the bias is predominantly negative and widespread (0.6–0.9 mm $day^{-1}$; e.g., in the BCC-CSM2-MR, BCC-ESM1, CESM2-WACCM, FGOALS-g3, MCM-UA-1-0, SAM0-UNICON). Over the vast swaths of the western United States, the models generally portray positive bias (~0.3–0.6 mm $day^{-1}$; as in the E3SM-1-0, E3SM-1-1, E3SM-1-1-ECA, GFDL-ESM4, GISS-E2-1-H, INM-CM5-0, IPSL-CM6A-LR, MRI-ESM2-0, NESM3). The annual mean precipitation simulations in the eastern United States are relatively good in many models (e.g., BCC-CSM2-MR, BCC-ESM1, CESM2-FV2, the three E3SM models, KACE-1-0-G, the two MPI models, NorESM2-LM), while being overestimated in others (INM-CM5-0, IPSL-CM6A-LR, MRI-ESM2-0, NESM3). The CMIP6 MMM has systematic biases mostly of the same sign but weaker amplitude: there are wet biases in the western half of the country, and dry biases along the Gulf Coast. For reference purposes, the annual mean precipitation assessed in twenty CMIP5 historical model simulations is shown in Supplemental Fig. 1, which reveals a similar structure of the bias patterns. This indicates significant model deficiencies in simulating precipitation across the contiguous United States.

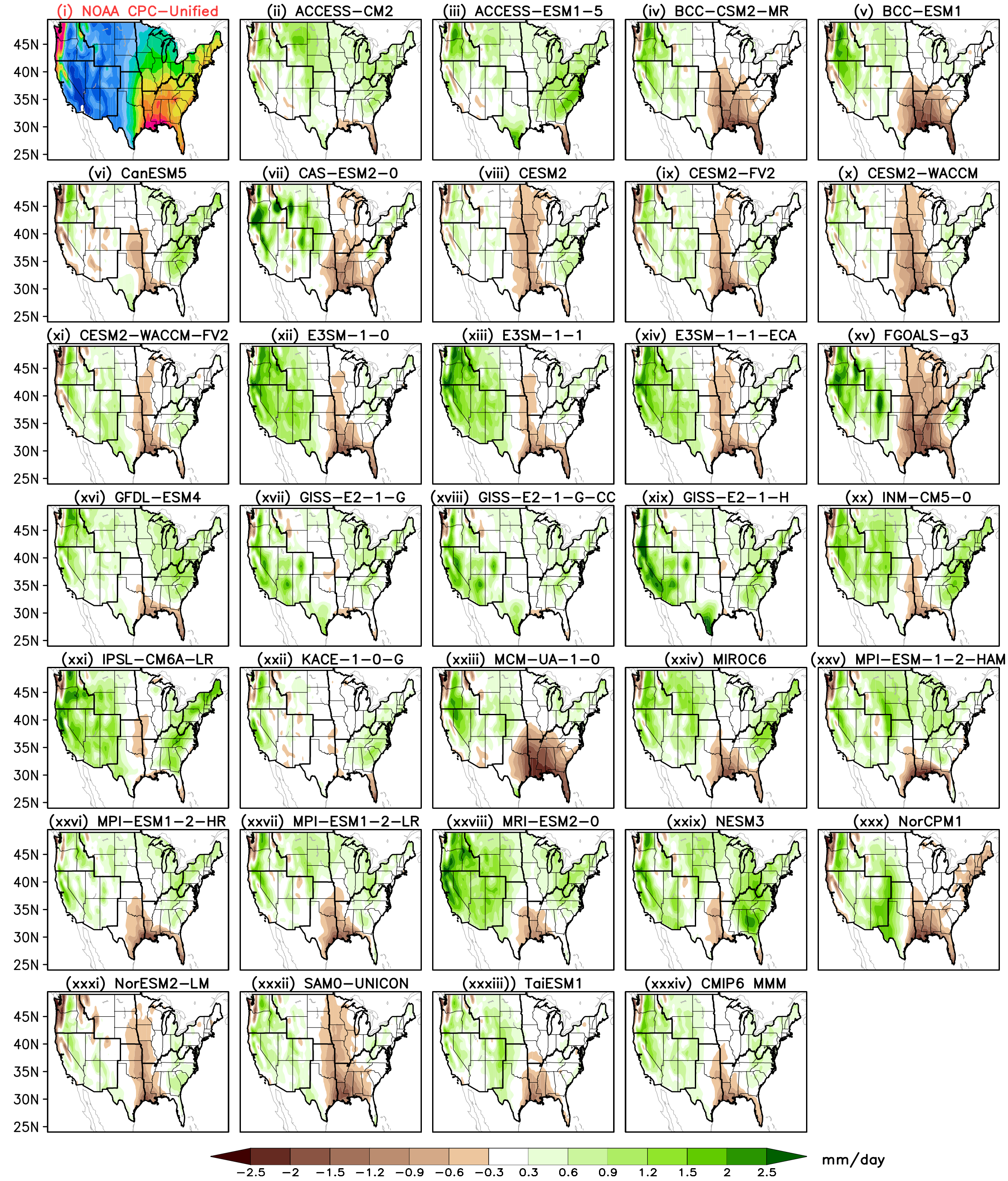


Fig. 3. The biases in the simulated annual-mean precipitation (mm day$^{-1}$) from the historical climate model simulations (1981–2010) of the 32 CMIP6 models analyzed in this study. The climatological precipitation from NOAA CPC-Unified — the observational target — is shown in the top-left panel; contour threshold and shading follow the same convention as Fig. 2 (left column). Annual mean rainfall is contoured and shaded at 0.3 mm day$^{-1}$ interval for values up to +/-1.5 mm day$^{-1}$, and at 0.5 mm day$^{-1}$ for higher values. The biases in the CMIP6 MMM with respect to the observational reference is shown in bottom-right panel.

The model-to-model and model-to-observations agreement in CMIP6 and CMIP5 for the annual mean of precipitation is displayed in Fig. 4 through a display of its area-averaged mean over the contiguous United States (CONUS; Figs. 4a-b), pattern correlation, and standardized deviation (Figs. 4c-d). Although there exist discrepancies on a regional scale (cf. Fig. 3), the CMIP6 model representation of the area-averaged values over CONUS is within 15% of the observed value. The bias in the CMIP5 MMM is slightly larger (an overestimation by ~20%). In general, however, most CMIP6 and CMIP5 models overestimate the magnitude of overland-mean precipitation. The model skill in replicating the observed spatial pattern varies widely amongst the GCMs, with the correlation coefficients in the range of 0.3–0.8 for CMIP6, and 0.2–0.5 for CMIP5. Almost all models overestimate the magnitude of the spatial variability of precipitation as displayed by the standardized deviations (Figs. 4c-d). From the CMIP6 models, the NorESM2-LM exhibits the highest correlation (0.76) and the smallest magnitude of bias (Fig. 4a), as well as yielding a smaller RMSE than other GCMs. Please note that the distance between the REF and individual model points represents the RMSE in a Taylor diagram (Taylor 2001). INM-CM5-0 and CESM2 exhibit higher correlations (0.75 and 0.70) than other CMIP6 models albeit with large RMSE (Fig. 4c); CESM2, however, shows relatively small bias (Fig. 4a). Amongst the CMIP5 models analyzed, the MPI-ESM-MR yields the highest correlation coefficient (0.51) in simulating the spatial pattern followed by FGOALS-g2 (0.49) and the CanCM4 (0.47) models; however, the RMSE in these CMIP5 models is much higher than the leading CMIP6 models.

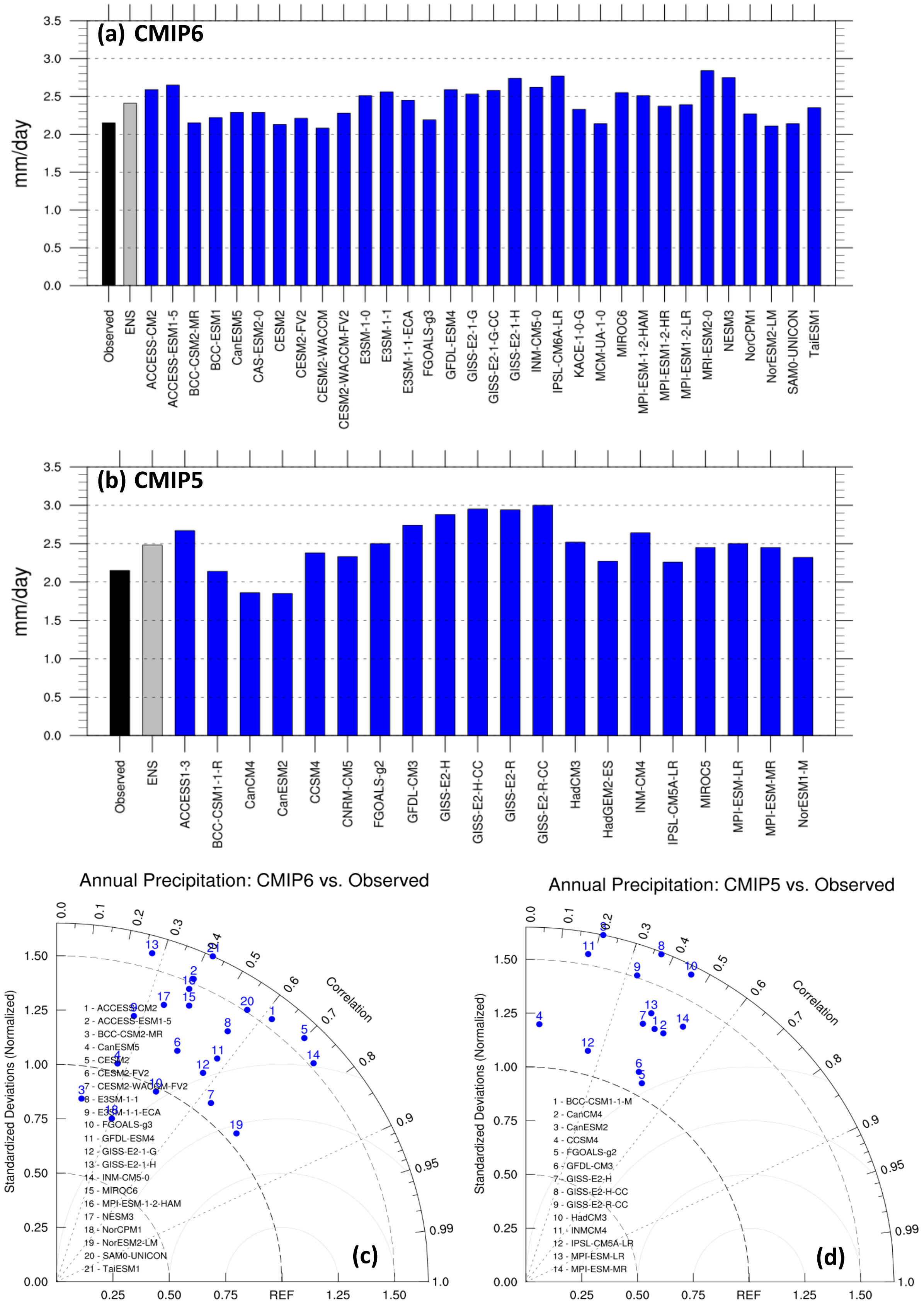


Fig. 4. Comparison of the observed and model-simulated annual mean precipitation in the analyzed CMIP6 and CMIP5 models. The area-averaged precipitation (mm day$^{-1}$; over land

surface only) are shown with respect to the observed (from CPC-Unified) data in (a) and (b). The spatial pattern correlations and standardized deviations are shown in panels (c) and (d) using Taylor diagrams (Taylor 2001). The distance between the REF point and individual model values (blue dots) represents the model RMSE.

### 3) Simulation of the Annual Cycle of Precipitation

The annual progression of monthly precipitation is presented in Fig. 5a-g through a display of its annual cycle in the seven NCA regions. The mean variation of the annual cycle is represented by the solid thick/thin lines for observations/models while the upper and lower bounds of the green shading denote the $\pm 1\boldsymbol{\sigma}$ range about the observed mean for a given month. Notable features of the observed cycle include the maximum in the winter months (November–March) over the northwestern and southwestern United States, a peak in the summer months over the Northern and Southern Great Plains, and the U.S. Midwest.

Despite the large inter-model variation and the differing degree of accuracy in the CMIP6 models analyzed in the study, the MMM portrays the seasonality of precipitation, especially its phase, fairly well in most NCA regions. While the MMM captures the timing of the winter maximum over the Northwest NCA region (Fig. 5a), it significantly overestimates the amplitude by as much as 30% in the winter months. In the Southwest NCA region (Fig. 5b), almost all GCMs overestimate the observed precipitation with the MMM coinciding with the upper bound of the $\pm 1\boldsymbol{\sigma}$ range of the observation. The annual cycle in the Northern Great Plains and the Midwest regions (Figs. 5c and e) is more realistic in the MMM, although it overestimates the summer peak in the former. The timing of the observed maximum in June over the Southern Great Plains (Fig. 5d) is also erroneous in the MMM, which peaks a month earlier in May. The weak annual cycle in the Northeast and Southeast NCA regions, where the observed variability is also considerably large, pose additional problems for the models, which display rather large inter-model fluctuations (Figs. 5f-g). The key finding here is that the variance of the models about the mean is almost directly correlated to the seasonal values, i.e., a high mean value often corresponds to high variance in the models independent of the region and the season.

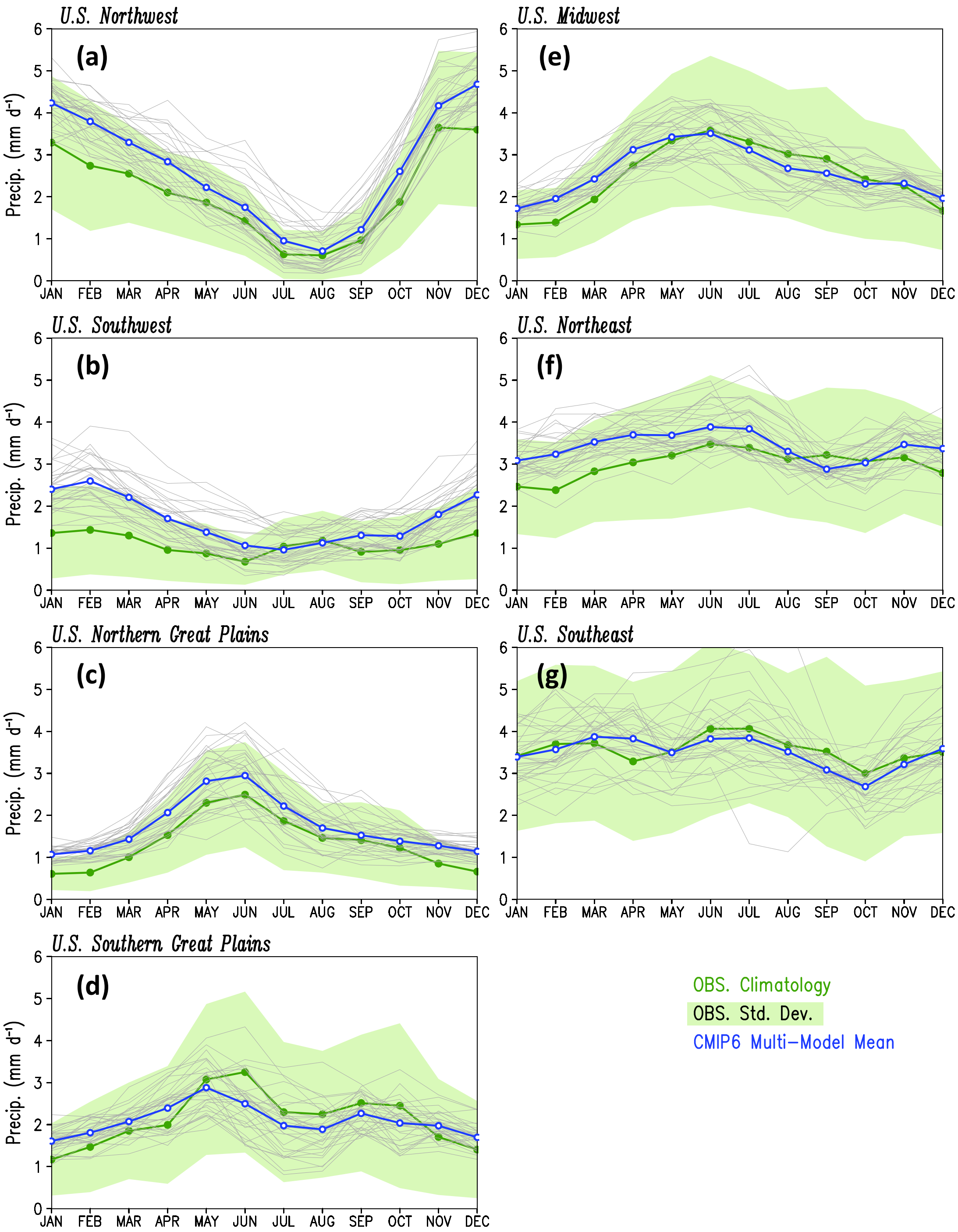


Fig. 5. The annual cycle of precipitation (mm day$^{-1}$) in the CMIP6 historical climate model simulations (1981–2010) for the seven U.S. NCA regions. The solid green line denotes the climatology from the observational target (NOAA CPC-Unified), while the green shading represents the ±1 standard deviations of the reference data. The annual cycle from the CMIP6 MMM is displayed using the solid blue line with open circles, while that from individual models are shown using thin grey lines.

The skill of CMIP6 models in simulating the annual cycle is further summarized for all the NCA regions using portrait diagrams in Figure 6. The fidelity of the CMIP6 GCMs in simulating the phase of the annual cycle, represented by correlation coefficients between the observed and simulations (Fig. 6a), is generally higher for the Northwest ($r$>0.90) and Northern Great Plains ($r$>0.80) compared to other NCA regions. Fig. 6a shows that the model skill is especially low in the Northeast and the Southeast NCA regions, where the correlation scores of many models are even less than 0.5. These results suggest that the models exhibit shortcomings in simulating precipitation in regions of elevated precipitation, e.g., the southeastern United States where an intensification of variability characterized by intense summer droughts and wet events in recent decades has been associated with greater equatorial Atlantic SST variability and SST warming (Wang et al., 2010). The normalized root-mean-square error (RMSE) plot (Fig. 6b) for the models reveals that the RMSE is < 40-50% of the observed mean for most NCA regions with the exception of the Southwest (normalized RMSE values greater than 0.7 in most GCMs). The correlation and normalized RMSE skill metrics reveal that the MMM consistently ranks among the best performers compared to individual models (cf. last column entries in Fig. 6a, b).

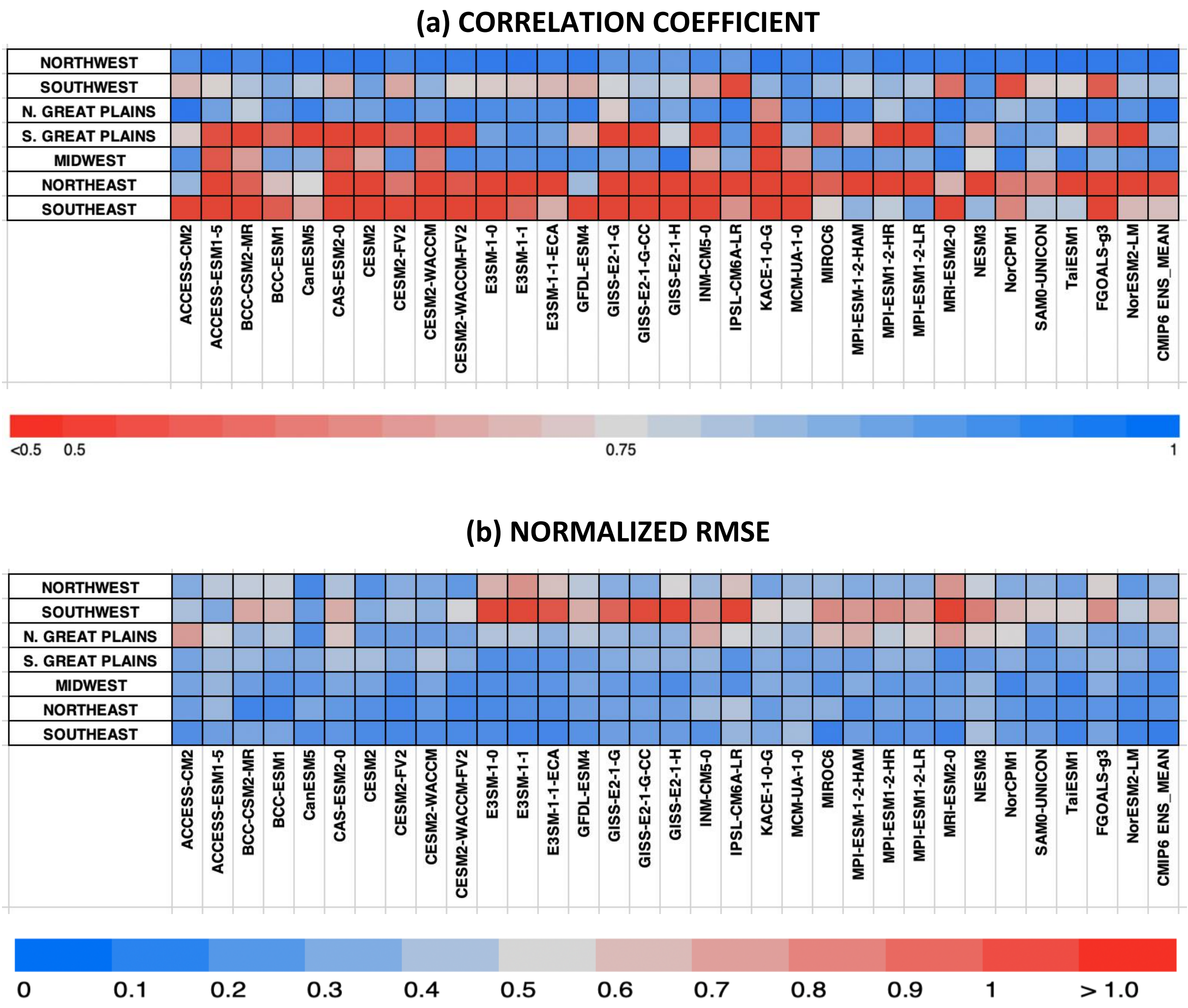


Fig. 6. Comparison of the model simulated annual cycle of precipitation in the 32 CMIP6 coupled climate models for the 1981–2010 period over the seven NCA regions of the CONUS. The correlation coefficients between the simulated and the observed annual cycle are shown in the upper panel. The RMSE normalized by the observed annual-mean values is shown in the bottom panel.

*b. Evapotranspiration*

The fidelity of CMIP6 coupled models in simulating evaporation is examined in Figure 7; the target benchmark for the evaluation is the ERA5 reanalysis, whose climatology is shown on the left panel for reference. Evapotranspiration follows the seasonal cycle of solar radiation and vegetation growth, attaining a peak in the summer months with a minimum in the winter (Fig. 7, left panel), in accordance with the findings of Rodell et al., 2015, their Fig. 4.

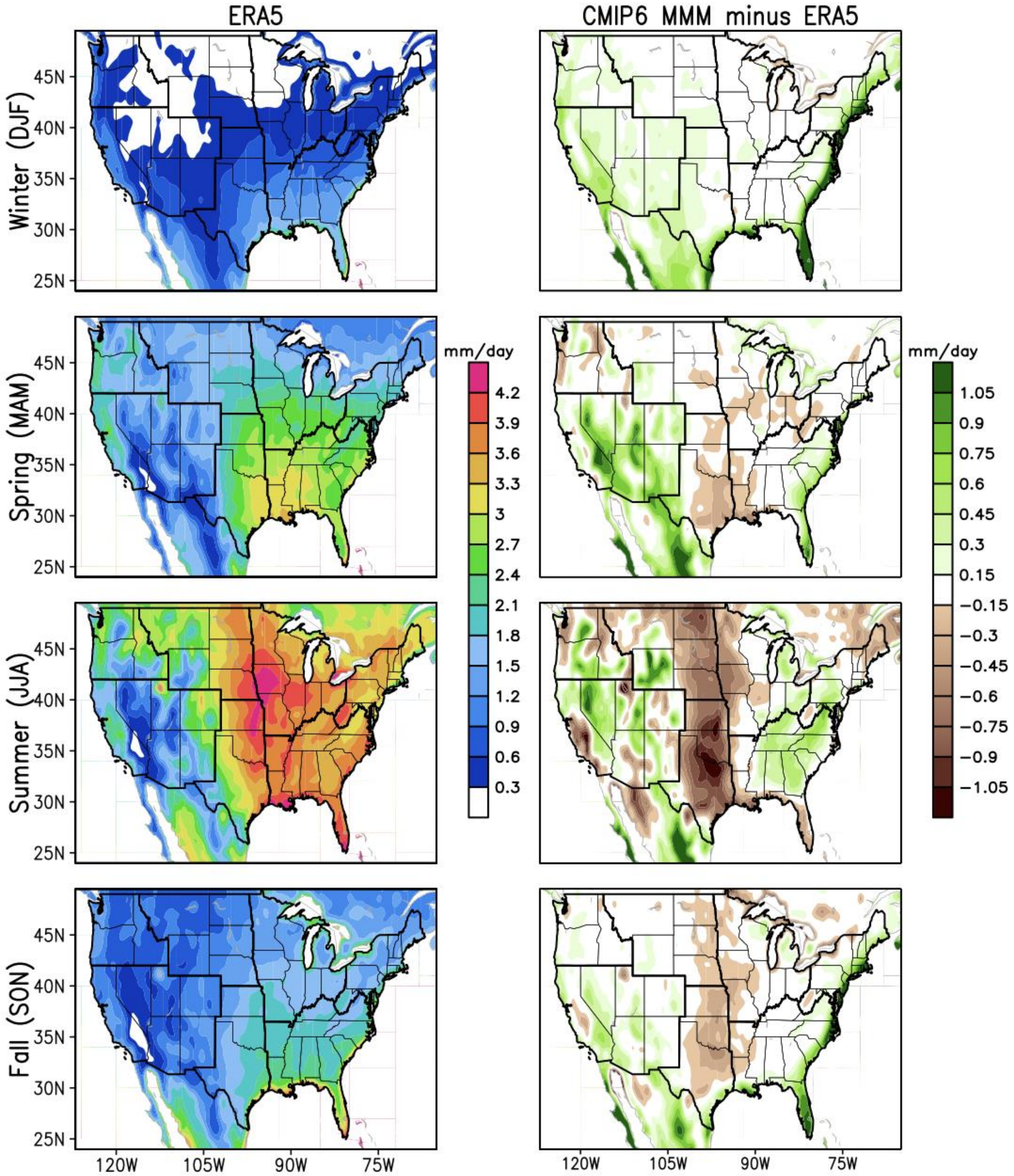


Fig. 7. Seasonal mean evapotranspiration (mm day$^{-1}$) over the CONUS for the reference dataset (ERA5 Reanalysis; left panel) and departure of the CMIP6 MMM from the observed (right panel). Results are shown for winter (December–February), spring (March–May), summer (June–August), and fall or autumn (September–November). The period of analysis is 1981–2010.

Evapotranspiration in the CMIP6 MMM of its coupled simulations exhibits varied biases, most notably a dry bias (~ 0.6–0.9 mm/day) in the summer in the Northern and Southern Great Plains, extending into the Midwest. Interestingly, the spatial structure of evaporation biases bears a close resemblance to that of its precipitation counterpart in summer (cf. Fig. 2, middle panel). The departure from the observed evapotranspiration is more modest in the fall and winter seasons, whereas spring is marked by the advent of dry bias over the southern states in addition to an overestimation over the Southwest NCA region (~0.75 mm/day).

*c. Moisture fluxes*

The vertically integrated moisture fluxes and their associated convergence/divergence assessed from ERA5 reanalysis and in the CMIP6 MMM in winter and summer seasons are shown in Fig. 8. There is a striking dissimilarity in the convergence fields over the contiguous U.S. between these two seasons. In winter, intense zones of moisture flux convergence (red shading) dominate along the U.S. west coast, and eastern and southeastern parts of the country, whereas divergence centers are situated offshore. In summer, although the moisture fluxes are moderate (cf. vectors in JJA panel, Fig. 8), there are broad swaths of weak divergence/near-zero convergence (blue shading) located over land. Consistent with Watterson et al. (2020; their Fig. 3) and Ryu and Hayho (2013), the summer moisture flow is part of the North Atlantic Subtropical High, the western branch of which carries moisture from the Gulf of Mexico to the eastern half of the country via the Great Plains Low-Level Jet (GPLLJ). Significant intensity increases in the GPLLJ are expected, concentrated in spring and autumn (Zhou et al. 2020).

Simulated moisture fluxes are in broad agreement with the reanalysis target with zonal moisture flow dominant in the winter season, and anticyclonic flow persistent over the South and Southeast in summer. In winter, the structure of the maximum moisture flux convergence zones is mostly in line with ERA5, although the MMM overestimates (by 1–2 mm/day) the magnitude of convergence over the Northwest and the Southwest NCA regions. The simulated moisture flux convergence by the CMIP6 MMM in summer is of the opposite sign (convergence) compared to ERA5 (weak divergence or, near-zero convergence) over the Northeast NCA region.

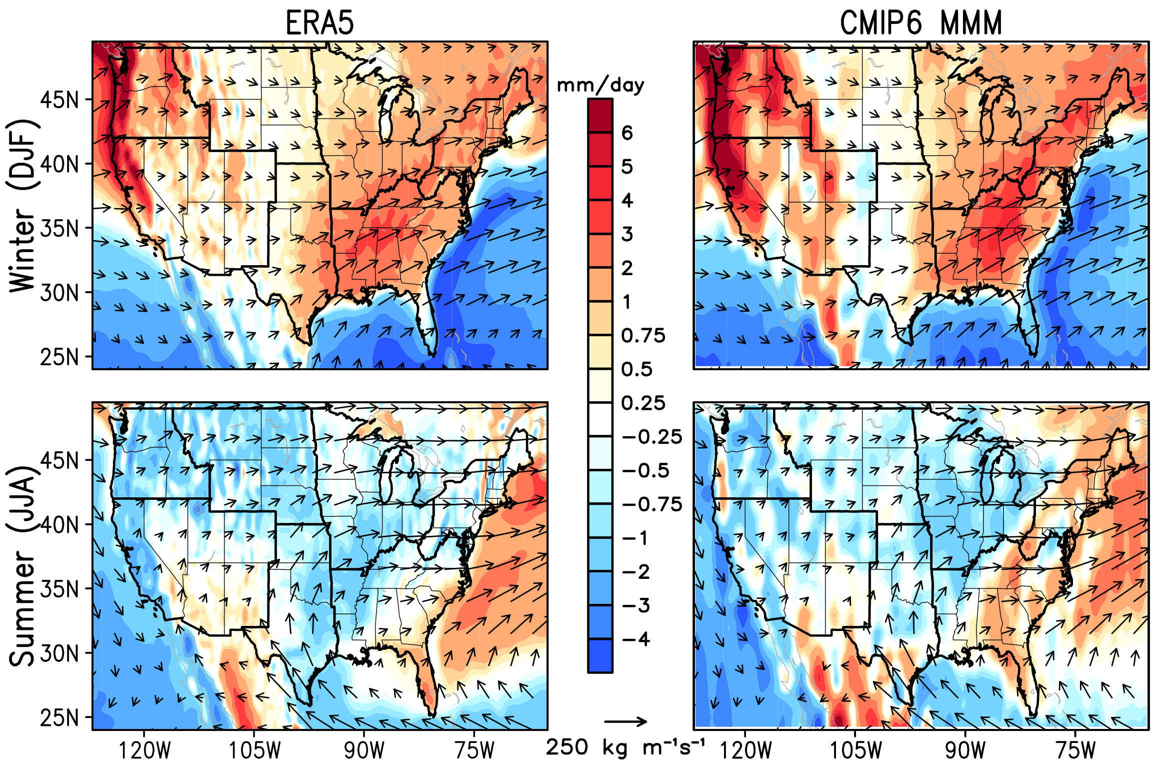


Fig. 8. Climatological means for horizontal moisture flux and its convergence/divergence during two seasons: (top) winter (December–February) and (bottom) summer (June–August), in the reference (ERA5 Reanalysis; left) and CMIP6 MMM (right). Moisture fluxes and corresponding flux convergence/divergence fields are vertically integrated. In all panels, vectors represent the moisture fluxes, with the reference vector being 250 kg $m^{-1}$ $s^{-1}$. Moisture flux convergence is shaded, with positive (red) and negative (blue) shading representing convergence and divergence respectively. The period of analysis is 1981–2010.

### *d. Precipitable water*

The evaluation of precipitable water (prw) in CMIP6 historical simulations is shown in Fig. 9 for the winter and summer seasons. In nature, prw is muted in winter with relatively low values (5–10 kg $m^{-2}$) prevailing over the CONUS, with largest values in the Southeast (~12.5–17.5 kg $m^{-2}$). In summer, high values (> 35 kg $m^{-2}$) of prw are observed in the Southern Great Plains and Southeast, likely related to moisture inflow from the Gulf of Mexico, as also noted in Fig. 8 earlier, and consistent with the findings of Watterson et al. (2020); their Fig. 2. The model differences (Fig. 9) reveal inaccuracy in terms of capturing the high prw values over the southern states in summer. The most notable MMM dry bias, of the order of 1-2 kg $m^{-2}$, occurs in the areas of the Southwest affected by the North American Monsoon. However, the MMM shows better skill in simulating prw in the winter, spring, and fall seasons. Fig. S2 (of the Supplemental Material) displays the climatological prw and model differences in the latter two seasons.

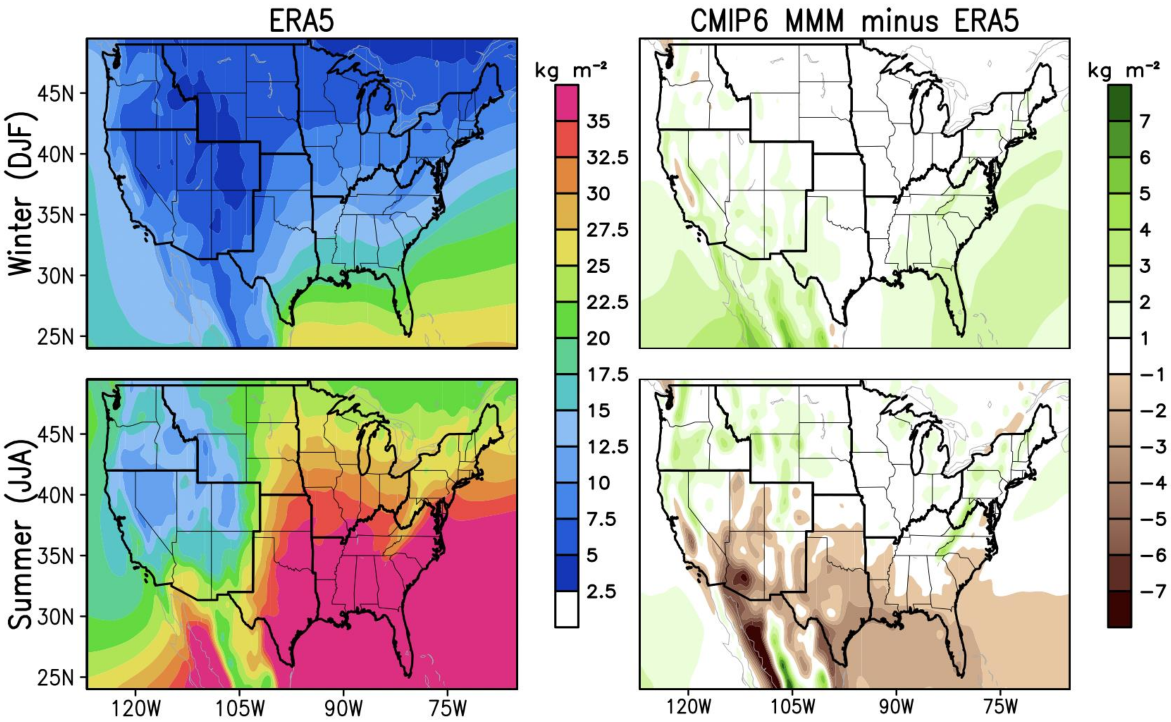


Fig. 9. Same as Fig. 7, but for precipitable water (prw; in units of kg $m^{-2}$) during two seasons: (top) winter (December–February) and (bottom) summer (June–August).

*e. Atmospheric water budget in the NCA regions*

In this section, the relative contributions of the local land surface processes and remote sources in producing precipitation are discussed for the models over the seven NCA regions and contrasted with observations/reanalysis. While it is important for climate models to have a robust simulation of precipitation, it is perhaps even more essential to assess if the remote and local processes responsible for producing precipitation are well-simulated. Here, an area average of the three water budget terms—precipitation (P), evapotranspiration (ET), convergence of vertically integrated moisture flux (MFC)—are computed for each NCA region. The column moisture tendency term, which is typically small and providing only a small contribution to the budget equation, is not separately diagnosed. Instead, the balance or residual (RES = P – ET – MFC) is assessed and compared against the observed/reanalysis data for each region; all shown in Fig. 10.

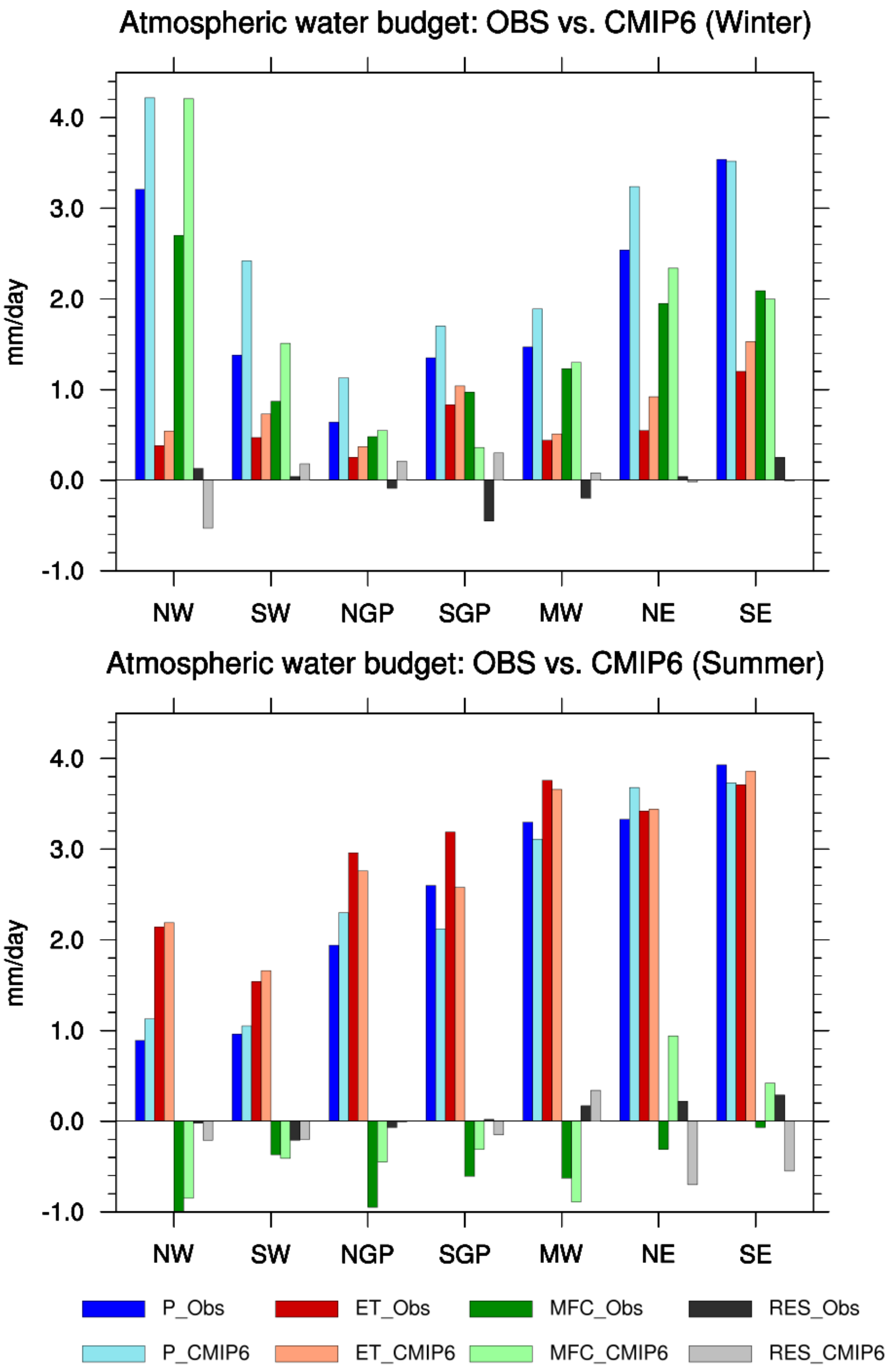


Fig. 10. Seasonal mean atmospheric water budget (in mm day$^{-1}$) from observations and CMIP6 MMM during two seasons: (top) winter (December–February) and (bottom) summer (June–August). Here, P is precipitation, ET is evapotranspiration, MFC is the vertically integrated moisture flux convergence, and RES = (P – ET – MFC) is the residual. The period of analysis is 1981–2010.

Results show that in winter, the moisture flux convergence dominates over evapotranspiration in the generation of precipitation in all of the seven NCA regions. The former term accounts for up to 80% of the precipitation in the Northwest and the Northeast, while the latter accounts for ~12% and 20% of the precipitation. MFC during the winter also accounts for up to up to 60% of the precipitation in the Southwest and Southeast, while evapotranspiration accounts for ~33% in both these regions. Interestingly, these areas also happen to be the zones of core winter precipitation (cf. Fig. 2 above) due to their moisture capacity and the positioning of storm tracks. During the summer, recycling of precipitation through land surface processes dominates the moisture budget terms. Evapotranspiration is the greatest in the eastern and northern parts of the country (aggregating between 2.7 mm/day and 3.8 mm/day), where precipitation is highest and vegetation thickest. The summer climatological P – ET is negative in six of the seven NCA regions (Fig. 10), consistent with previous studies (e.g., Baker and Huang 2014, their Fig. 6); P and ET are almost comparable (3.93 mm/day and 3.71 mm/day respectively) in the Southeast. On the other hand, MFC during this season is of the opposite sign (implying moisture flux divergence) and much smaller in magnitude (ranging between 0.10 mm/day and 1.2 mm/day) compared to ET across all the NCA regions in the ERA5 reanalysis. The moisture budget equation is almost balanced (RES ~ 0) across the NCA regions in the observed, which attests to the smallness of the column moisture tendency term.

The realism of the atmospheric water balance in the models is also investigated in Fig. 10. Over the Northwest and the Southwest, where remote influences play a more vital role in generating winter precipitation than local processes, MFC is overestimated by almost 55% and 70% in the CMIP6 MMM (climatological MFC values are 2.7 mm/day and 0.9 mm/day respectively). As a result of these variations, the model moisture budget equation is unrealistic, especially in the Northwest (RES ~ -0.53 mm/day). We, therefore, attribute the wet bias in winter precipitation (of about 30% and 70%) over the Northwest and the Southwest, noted also in Fig. 2, to model overestimation of remote moisture fluxes in addition to lack of resolution of orography.

During summer, when the land surface processes via ET dominates over MFC, the models underestimate ET in the Southern Great Plains by 24% (as also seen earlier in Fig. 7, JJA panel for model differences); here, the background climatological ET is 3.19 mm/day respectively. The negative MFC in the Southern Great Plains is also underestimated by about 50% in summer; model simulated value is 0.31 mm/day against a climatology of 0.61 mm/day respectively. Based on these two findings, we conclude that the summer precipitation deficit noted over the Southern Great Plains (in Fig. 2) results primarily from an underestimation of local processes (ET) as well as remote influences (MFC) – the former term playing a more influential role over the latter in summer. The assessment also suggests that although the MMM accurately portrays the ET field in the Northeast and Southeast during summer, the observed weak moisture flux divergence is not captured; rather, the term is positive implying moisture flux convergence. Please note that although taking an area average is beneficial in summarizing the water budget terms over the NCA regions, the aggregated numbers may mask out important variations at subregional scales, particularly in cases where regions contain fields of opposite sign, as for the Southeast MFC in summer (cf. Fig. 8).

## 4. Uncertainty in water cycle simulations

The simulations of the twentieth century (i.e., historical) climate provide avenues for the evaluation of models whose future projections directly inform IPCC's Assessment Reports. Before estimating the sign and magnitude of future changes of the regional water cycle, it is important to assess the degree of agreement among the models in representing the historical period, especially for quantities having reliable, long-term observations. Among the atmospheric water budget terms, simulations of precipitation and evaporation have better observational constraints and will be of primary focus in this section. Previous studies (e.g., Waliser et al., 2007) have documented that that model representation of these quantities also benefits from indirect constraints, such as connections between the energy (via top-of-the-atmosphere energy balance) and water cycles.

Figs. 11 and 12 show a measure of model performance with respect to observations as well as the level of agreement among the models across each of the seven NCA regions for precipitation and evapotranspiration respectively. In the upper panels (a-b), the box for each NCA region contains data between the 25$^{th}$ and 75$^{th}$ percentile (i.e., 50% of the data), while the dashed line in the vertical encompasses the range between the minimum and maximum values of the simulated quantities in the models. Looking at Fig. 11 (upper panels) and focusing on where the box plot for the distribution of modeled values lies vis-à-vis the observational target (red asterisk), the greatest model underperformance is seen in the winter, especially in the Northwest, Southwest, Northern Great Plains, and the Northeast; the observed (target) values here are even outside the upper and lower bounds of the model-simulated values.

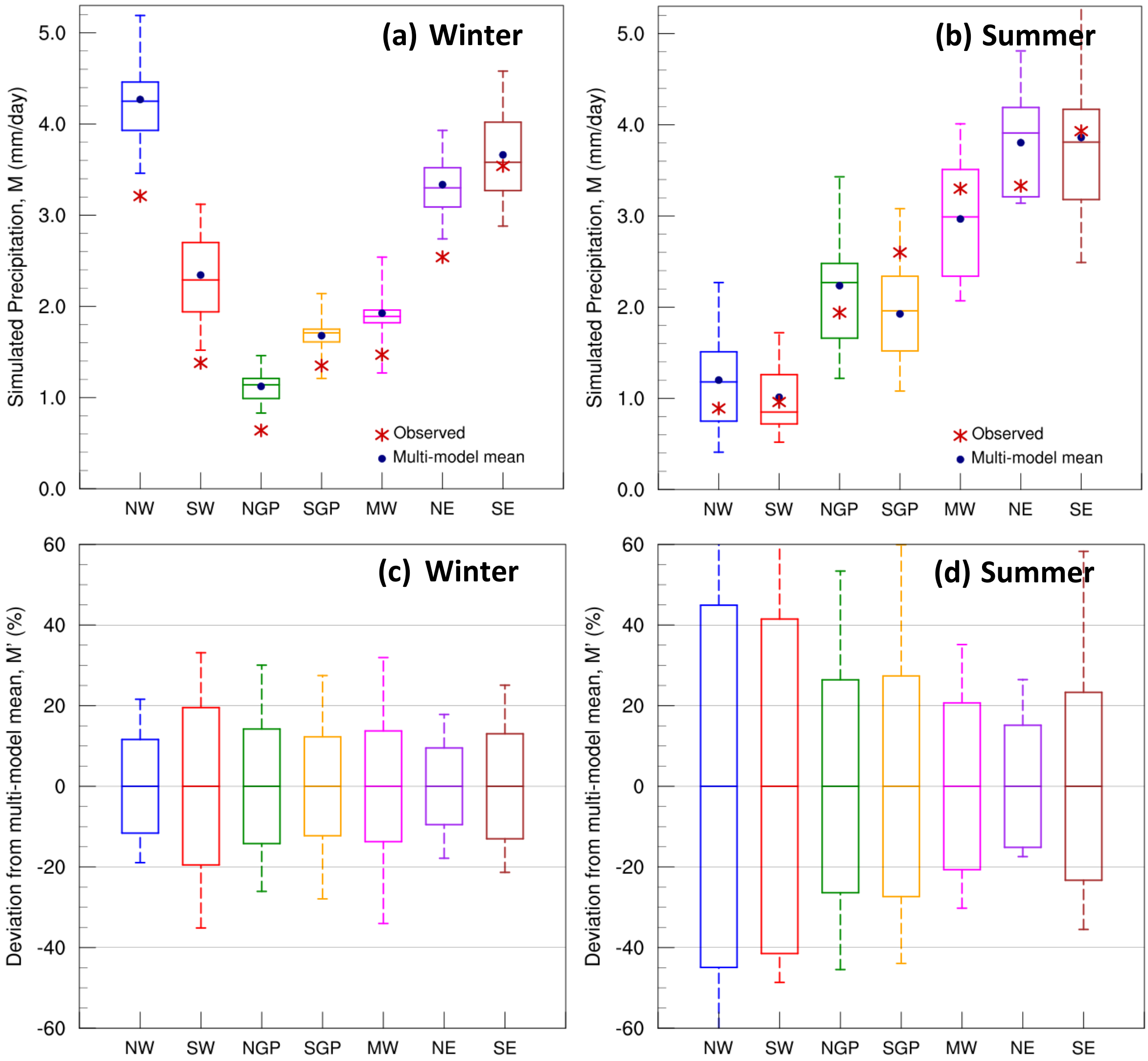


Fig. 11. Uncertainty in the historical simulations of precipitation in the CMIP6 models assessed for this study over the seven U.S. NCA regions displayed using two different measures: (upper panel) model spread about the observed mean, and (lower panel) model-to-model agreement in the simulated mean values. The period of analysis is 1981–2010 for two seasons: (left) winter (December–February) and (right) summer (June–August). For the upper panel, the minimum, 25$^{th}$ percentile, median, 75$^{th}$ percentile, and maximum values of simulated precipitation are shown for each box-whisker plot. Also, shown are the climatological mean from the observed (using red asterisks) and the multi-model mean (using blue solid dots). For the lower panel, model disagreement is displayed using deviations (M') of individual model values (M) from the multi-model mean ($\bar{M}$), where, $M' = \frac{(M - \bar{M})}{\bar{M}} * 100\%$. The box plot here shows the maximum and minimum values of M', represented by the ends of the error bars, while the box that extends about zero denotes the $\pm 1$ standard deviation of M'.

In the summer, the distribution of historical simulations and their multi-model mean are closer to the observations, except for the Southern Great Plains. Thus, we can conclude that the range of simulated precipitation conforms more closely with observations in the local summer compared to the winter. For the lower panels (c-d), the multi-model mean, $\overline{M}$, is computed from the distribution of individual modeled quantities, $M$. Thereafter, the deviation of each model's value from the multi-model mean, $\overline{M}$, is computed as: $M' = \frac{(M - \overline{M})}{\overline{M}} * 100\%$. The box plot here represents the maximum and minimum deviation in these modeled values from the multi-model mean (shown as the ends of the error bars), and the standard deviation in $M'$ (as the box that extends about zero). This inter-model agreement analysis follows the strategy outlined in Waliser et al. (2007). The bottom panel of Fig. 11 indicates that the model disagreement (as a measure of standard deviation) for regionally averaged precipitation is roughly $\pm$20% in winter, and $\pm$40% in summer. The Northwest and Southwest, which are climatologically dry in the summer, have the largest deviations from $\overline{M}$, possibly indicating sensitivity to the model outliers; for instance, the maxima in the modeled value in NW summer is ~2 times greater than $\overline{M}$ (Fig. 11b) which would lead to a much higher $M'$. Based on the lower panels of Fig. 11, we can draw the following conclusions. First, the inter-model agreement is greater in the winter compared to summer. Second, a better model agreement is observed where climatological values are higher. This is possibly due to differences in spatial scales of the precipitation generating mechanisms, e.g., synoptic in winter, and convective in the summer.

Shifting the focus to evapotranspiration (Fig. 12), the distribution of model simulated values mostly reveals an overestimation vis-à-vis the observational targets (red asterisk) in the winter. ET, however, is mostly muted in this season with climatological values <1.2 mm/day across the NCA regions. In summer, the box plots for model representation of ET containing data between the 25$^{th}$ and the 75$^{th}$ percentile encompasses the climatological values (red asterisks). The Northern and Southern Great Plains are an exception, where most models and in particular, their multi-model mean (blue solid dots), underestimate the climatological values. Thus, from the upper panels of Fig. 12, we can conclude that the distribution of model simulated ET agrees more closely with the observational targets across the NCA regions in summer than in winter. The lower panels of Fig. 12 display the level of inter-model agreement in simulating regionally averaged ET for winter and summer seasons. In winter, the model disagreement (as a measure of standard deviation) is greatest (roughly $\pm$30-40%) for the Northwest, Northern Great Plains, and the Midwest, and least ($\pm$10-20%) for the Southern Great Plains and Southeast, which are also most active in terms of ET in this season (climatological values are ~0.8 mm/day and 1.2 mm/day respectively). In summer, the model disagreement is of the order of ±15-25% across the seven NCA regions. In conclusion, the inter-model agreement is greater in summer for ET compared to winter; this is contrary to the finding for precipitation in Fig. 11. Second, the eastern NCA regions (Northeast, Southeast) exhibit greater model agreement in simulated ET relative to the other regions.

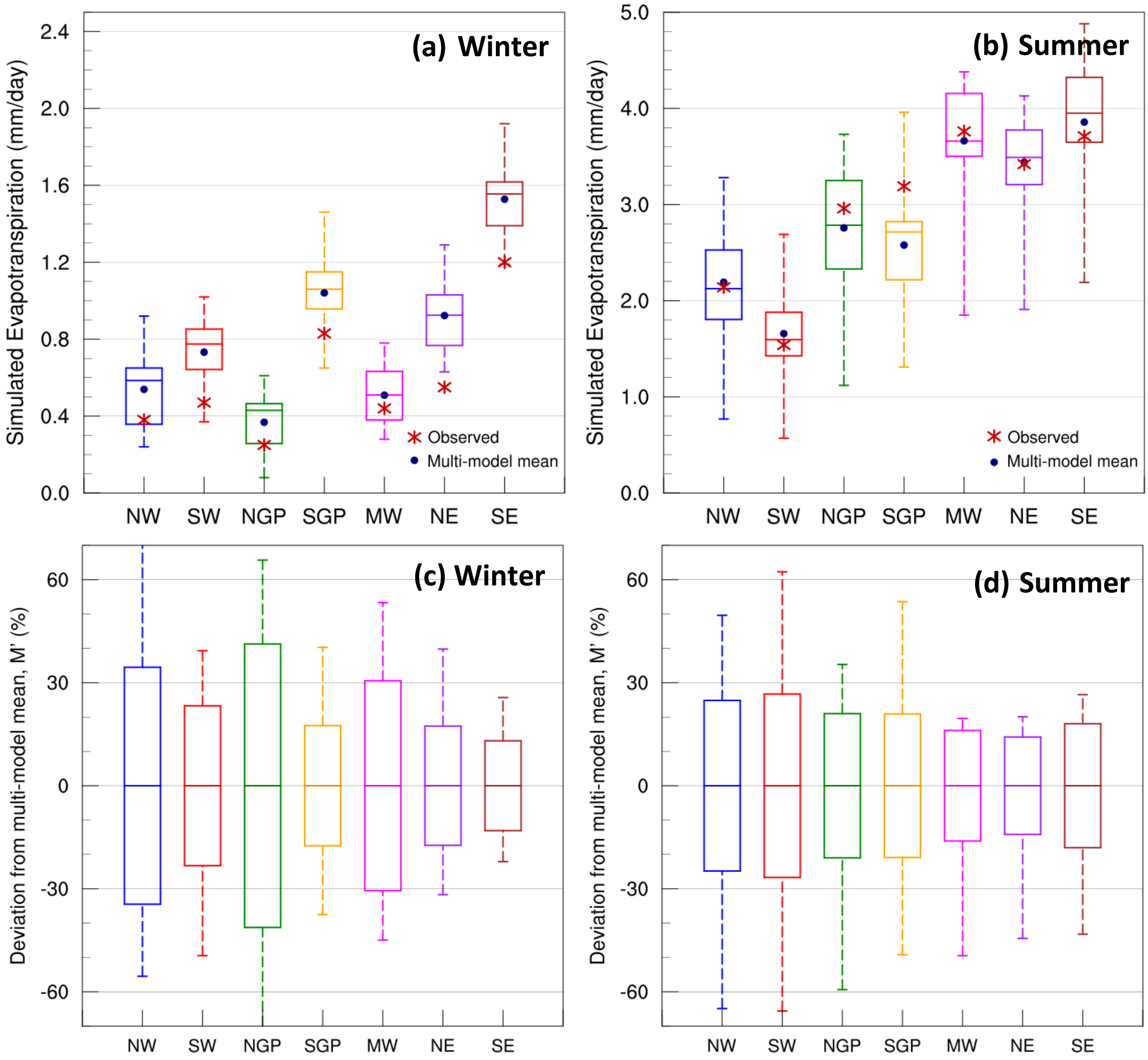


Fig. 12. Same as Fig. 11, but for model simulations of evapotranspiration.

## 5. Projected future changes and associated uncertainty

In this section, we examine the future changes in precipitation by region and by seasons, as projected by the global climate models whose historical simulations are the focus of investigation in the previous sections. Figure 13 shows the simulated historical mean and the projected changes (2071–2100 relative to 1981–2010) in the seasonal precipitation and 850-hPa winds over each NCA region according to CMIP6. Over the western and northeastern United States, the projected winter precipitation is characterized by increases in the future. Precipitation is projected to increase in the Northwest by 0.4 mm/day (historical mean is 3.0–4.2 mm/day), in northern California by 0.6 mm/day (against a base climatology of >4.2 mm/day), and in the Northeast by 0.8–1.0 mm/day (historical climatology of 3.0–3.3 mm/day). The projected increase is consistent with the increase in cyclonic circulation over the east coast, characterized by amplified easterlies and southeasterlies which facilitate enhanced moisture transport. The enhanced precipitation in spring is mainly concentrated over the Midwest and Northeast; increase of 0.6–0.8 mm/day relative to a historical climatology of 2.7–3.3 mm/day for the former, and 3.3–3.6 mm/day for the latter. The circulation pattern changes in this season tend to favor weakened zonal flow and enhanced southerly flow over these two NCA regions. In summer, the precipitation change is characterized by a meridional dipolar distribution with widespread drying in the Northern Great Plains (of the order of 0.2–0.4 mm/day) and the Midwest (by 0.2–0.6 mm/day), and increase in the Southeast (by 0.2–0.6 mm/day). The projected changes are generally in good agreement with the enhanced anticyclonic flow in the southeast transporting moisture from the Gulf of Mexico and weakened meridional southerly flow over the northern and midwestern states resulting in the precipitation decline. For the fall season, the projected precipitation changes are modest, localized over the Southeast and parts of the Northwest (0.4–0.6 mm/day). The results here are in good agreement with the previous CMIP5 based projections under the RCP8.5 scenario, reported in the Fourth NCA Report (USGCRP 2017, their Fig. 7.5), which favored an increase in winter precipitation over the northern and western swaths of the contiguous U.S., and decrease in summer precipitation in the northern Great Plains and the Midwest.

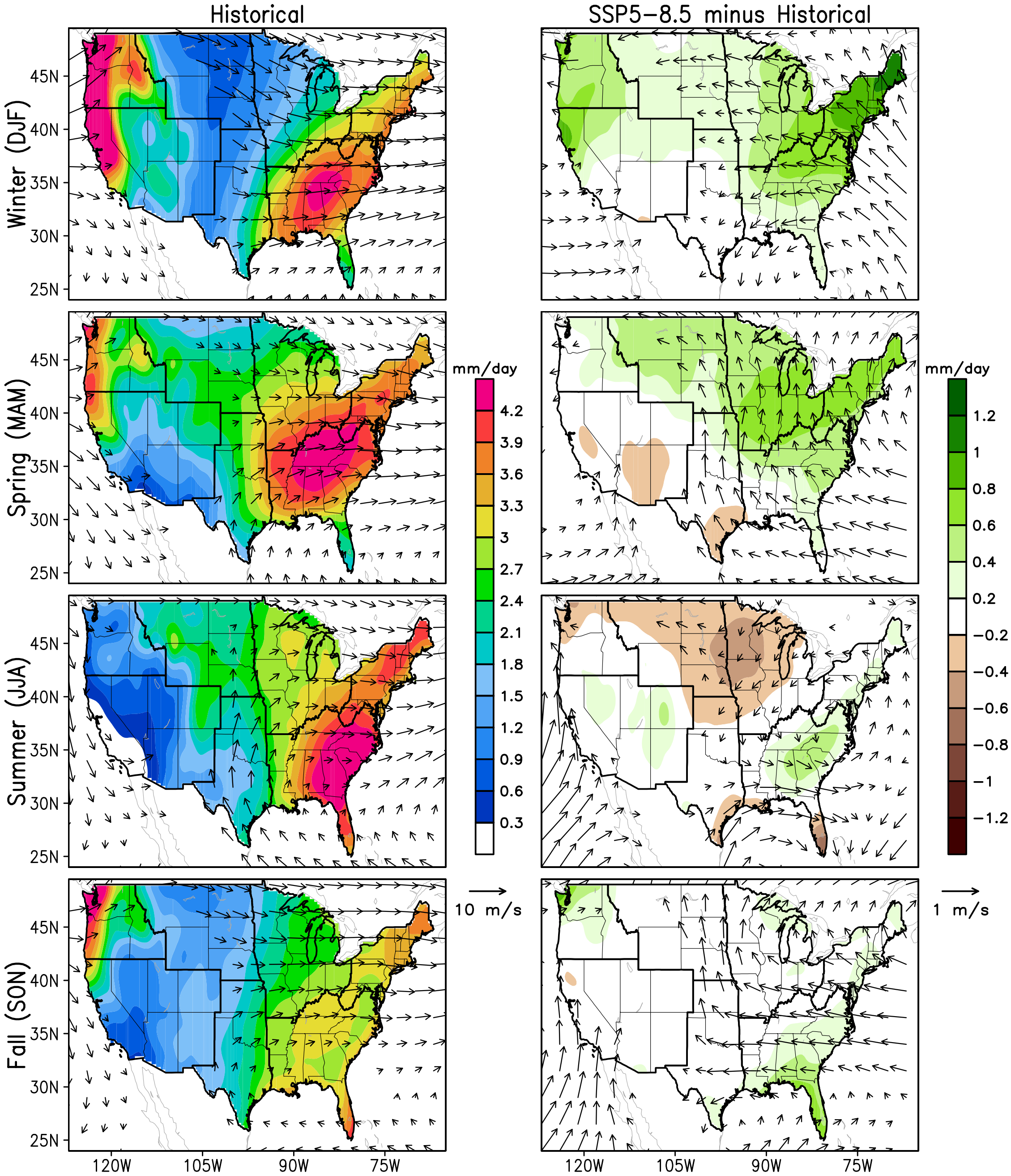


Fig. 13. Projected change in seasonal mean precipitation (shading; mm day$^{-1}$) and 850-hPa winds (vectors; m s$^{-1}$) from CMIP6 for the end-of-the-century (2071–2100) under the SSP5-8.5 scenario. The climatological mean in the CMIP6 MMM over the historical period (1981–2010) is shown on the left, and future change (2071–2100 relative to the 1981–2010 average) is shown on the right. Results are shown for winter (December–February), spring (March–May), summer (June–August), and fall or autumn (September–November).

The projected precipitation sensitivity (percentage change per Kelvin global mean surface air temperature change) under SSP5-8.5 is displayed in Fig. 14. The confidence level of the CMIP6 MMM results is presented via the lower and upper bounds of the box representing data between the 25th and 75th percentile, while the ends of the vertical dashed line denote the range between 5th and 95th percentile. In other words, the vertical dashed line encompassing 90% of the projected data represents the range of "very likely" future occurrence, as per definition presented in the IPCC Fifth Assessment Report (Mastrandrea et al. 2010). In winter, the projected mean precipitation very likely increases over five of the seven NCA regions (NW, NGP, MW, NE, and SE; their 90% ranges being above the zero line). The greatest precipitation sensitivities occur for NGP (6.17% $K^{-1}$) and NE (6.55% $K^{-1}$). Model agreement is also found for the spring projected precipitation change with very likely increases favored for the same five NCA regions noted above. Model uncertainty is more substantial over SW and SGP in winter and, even more so, in spring, with both positive and negative projected changes in the distribution of CMIP6 MMM projections. For summer, the models do not fully agree on the sign of the likely future occurrence for any of the NCA regions. The mean of the summer projected precipitation sensitivities, however, favor a decrease for NW (1.42% $K^{-1}$), NGP (3.12% $K^{-1}$), and MW (2.45% $K^{-1}$). Meanwhile, the NW and SW exhibit the largest inter-model spreads. The uncertainties in projected changes are also substantial in the fall season, with the models divided in terms of the sign of the projected sensitivities. The spreads of the modeled projected values are also large in this season ranging between -4% $K^{-1}$ and +7% $K^{-1}$. From Fig. 14, it is evident that the confidence in projected precipitation sensitivities, measured by the inter-model spread and the model agreement on the sign of projected changes, is the greatest for the winter season and least for the summer season over the CONUS.

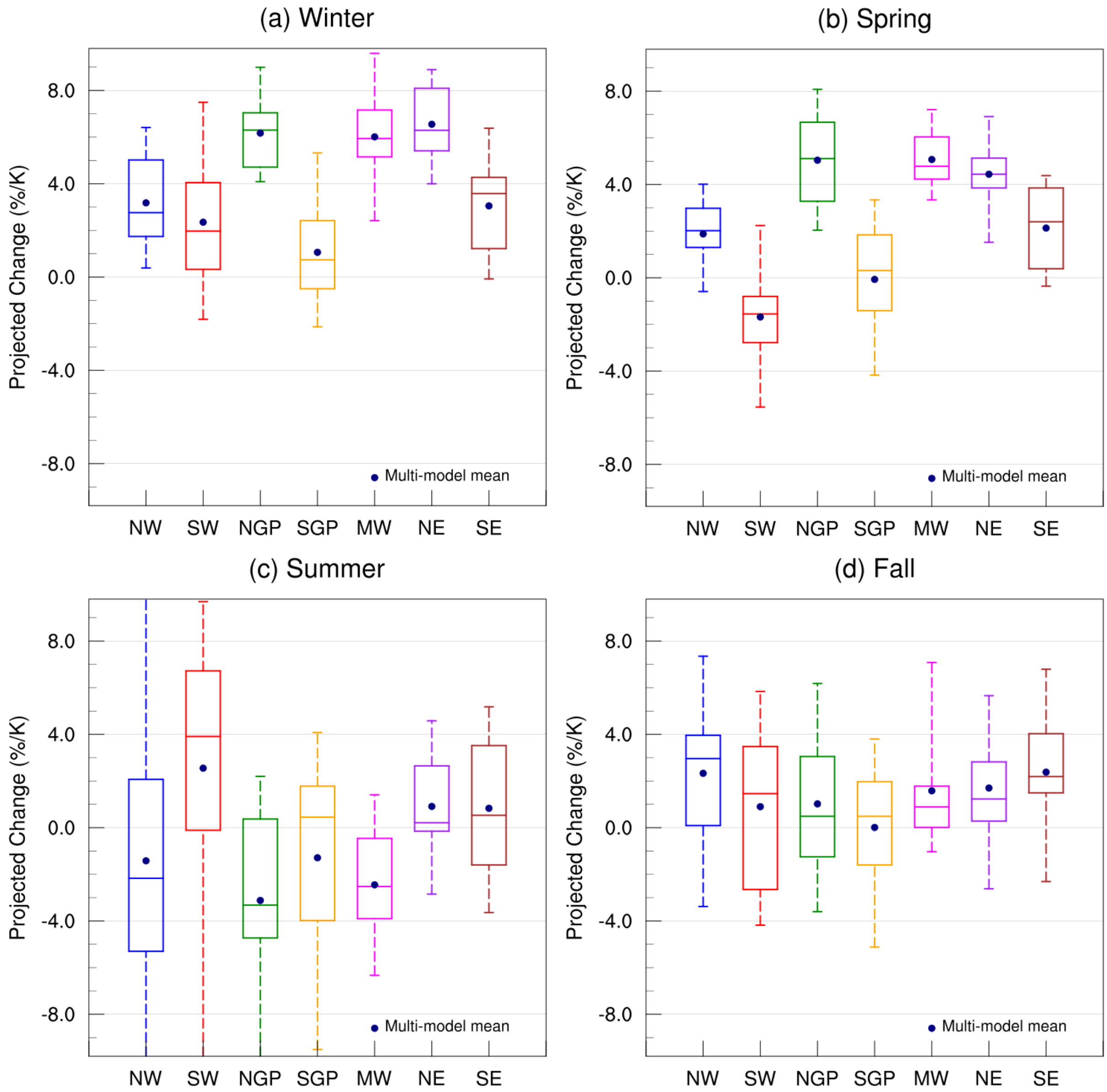


Fig. 14. Projected precipitation sensitivity under SSP5-8.5, i.e., the percentage change in precipitation (2071– 2100 relative to 1981–2010) per 1°C, or 1K global warming (% $K^{-1}$) derived from CMIP6 models for (a) winter, (b) spring, (c) summer, and (d) fall or autumn at each NCA region. In each subplot, the lower and upper ends of the box represent the 25$^{th}$ and 75$^{th}$ percentile, while the ends of the vertical dashed line denote the range between 5$^{th}$ and 95$^{th}$ percentile. The horizontal line within the box is the median, and the blue circle is the multi-model mean.

## 6. Summary and concluding remarks

The present study seeks to examine the structure of the atmospheric water budget components over the seven U.S. NCA regions and the extent to which the observed features are represented in the state-of-the-art climate model simulations. In this regard, attention is focused on the simulated variables available from the new CMIP6 archive, namely, precipitation, evapotranspiration, column integrated horizontal moisture transport and its convergence, and precipitable water. The main findings concerning the fidelity of CMIP to represent the nature and variability of seasonal and regional hydroclimate over the contiguous U.S. are as follows:

- Climatological winter precipitation is reasonably well simulated, with the exception of the mountains of the U.S. West (the Cascades and the Sierra), likely stemming from model deficiencies in the resolution of orography. Climatological summer precipitation is more problematic for the models as evidenced by the expansive deficit over the central Plains (Fig. 2).
- The CMIP6 models replicate the spatial pattern of the annual mean precipitation fairly well (Fig. 4; pattern correlations), while the annual cycle is considerably more challenging (Figs. 5 and 6). Models tend to overestimate the amplitude of the winter maxima in the Northwest and the Southwest while failing to capture the timing of the summer peak in the Southern Great Plains. Models exhibit large variance in regions and months of high mean precipitation.
- The simulated evapotranspiration bears a close resemblance to the ERA5 reanalysis counterpart, except for the summer season which exhibits a widespread dry bias stretching across the Great Plains (Fig. 7). A key finding is a similarity in the location of the ET dry bias with that of the corresponding one from precipitation.
- The CMIP6 model representation of the column integrated horizontal moisture flux convergence and the precipitable water are in broad agreement with the ERA5 reanalysis target. An interesting seasonal fluctuation is noted across the climatological winter and summer, with intense moisture flux convergence zones located over the land in the former and mostly weak divergence in the latter (Fig. 8).

The analysis strategy is precipitation-centric, and as such, revolves around the relative contribution of local (evapotranspiration) and remote (moisture flux convergence) water sources in the generation of precipitation. The relative importance of these two processes is compared in observations and simulations; the key findings are summarized below.

- In winter, the diagnosis of the atmospheric water budget reveals that the remote contributions via moisture flux convergence play a much more important role than local evapotranspiration in all seven NCA regions (Fig. 10; upper panel). In fact, it accounts for four-fifths of the precipitation received in the Northwest, and three-fifths in the Southwest. The CMIP6 MMM, however, overestimates the remote influence from the Pacific (cf. Fig. 8) for both these regions resulting in a wet bias in the winter mean precipitation.

- In summer, the local recycling of precipitation via evapotranspiration is larger than the convergence of moisture fluxes from remote regions (Fig. 10; lower panel). The CMIP6 MMM underestimates the local contribution of evapotranspiration in the Southern Great Plains, resulting in the expansive summer precipitation deficit noted above (cf. Fig. 2).
- The investigation into the uncertainty associated with the water cycle simulations over the CONUS demonstrates better inter-model agreement in regions and seasons when the climatological values are higher, e.g., for winter precipitation in the U.S. West (Fig. 11) and summer evapotranspiration in the East (Fig. 12).

Furthermore, this study provided an NCA-specific view into end-of-century precipitation changes over the CONUS. Under the SSP5-8.5 warming scenario, the CMIP6 models' projected changes are summarized as follows:

- There is high model confidence that the projected winter mean precipitation will very likely increase over five of the seven NCA regions (NW, NGP, MW, NE, and SE). The projected increase is consistent with an increase in cyclonic circulation over the East Coast which facilitates enhanced moisture transport from the Atlantic (Fig. 13). The greatest precipitation sensitivities are seen in NGP (6.17% $K^{-1}$) and NE (6.55% $K^{-1}$) (Fig. 14).
- In summer, the future projections exhibit a meridional dipolar distribution with a widespread decline in the Northern Great Plains and the Midwest and an increase in the Southeast. These changes are also supported by the circulation setup: enhanced anticyclonic flow in the Southeast transporting surplus moisture from the Gulf of Mexico and weakening of southerly flow into the northern and midwestern states (Fig. 13). Model confidence into the sign of the future projected precipitation sensitivity is, however, the least in the summer with both increases and decreases

projected across the suite of CMIP6 models, and often with large inter-model spread (Fig. 14).

In support of the upcoming NCA5 report, our present study provides a comprehensive diagnosis of the atmospheric water budget with quantitative model comparison, multi-model ensemble projections, and seeks to relay these projections from state-of-the-art coupled climate models to stakeholders with adequate uncertainty estimates. To the extent that uncertainty varies across variables, regions, and scales, our work helps foster the ability to discern which projections are most reliable and therefore usable in complex decision-making contexts, as well as identifying those aspects which need further observational and model-development work.

*Acknowledgments.*

This research was carried out at the Jet Propulsion Laboratory, California Institute of Technology, under a contract with the National Aeronautics and Space Administration. We acknowledge the climate modeling groups for making their model outputs available, the Program for Climate Model Diagnosis and Intercomparison for collecting and archiving CMIP data, and WCRP's Working Group on Coupled Modelling. A.S. would like to thank Dr. Alfredo Ruiz-Barradas for his help with providing the topography and bathymetry data.

*Data Availability Statement.*

All datasets used in this study are publicly available. The CMIP6 and CMIP5 model output data are available from https://esgf-node.llnl.gov/projects/cmip6/ and https://esgf-node.llnl.gov/projects/cmip5/ respectively. The precipitation datasets used for model evaluation: (i) NOAA-CPC Unified CONUS dataset is available from https://psl.noaa.gov/data/gridded/data.unified.daily.conus.html, (ii) PRISM dataset is available from https://prism.oregonstate.edu/, (iii) GPCC dataset is available from https://www.dwd.de/EN/ourservices/gpcc/gpcc.html, and (iv) the CRU TS4.02 dataset is available from https://crudata.uea.ac.uk/cru/data/hrg/cru_ts_4.02/. The ERA5 reanalysis data is downloadable from https://cds.climate.copernicus.eu. Topography data is available from https://www.ngdc.noaa.gov/mgg/global/.

# REFERENCES


Amante, C. and B. W. Eakins, 2009: ETOPO1 1 arc-minute Global Relief Model: Procedures, data sources, and analysis. NOAA Technical. Memo NESDIS NGDC-24, p. 25.

Baker, N. C., and H.-P. Huang, 2012: A comparison of absolute and relative changes in precipitation in multimodel climate projection. *Atmospheric Science Letters*, **13**, 174–179.

——, and ——, 2014: A comparative study of precipitation and evaporation between CMIP3 and CMIP5 climate model ensembles in semiarid regions. *Journal of Climate*, **27**, 3731–3749.

Barlow, M., S. Nigam, and E. H. Berbery, 2001: ENSO, Pacific decadal variability, and US summertime precipitation, drought, and stream flow. *Journal of climate*, **14**, 2105–2128.

Berrisford, P., and Coauthors, 2011: Atmospheric conservation properties in ERA-Interim. *Quarterly Journal of the Royal Meteorological Society*, **137**, 1381–1399.

Bosilovich, M. G., S. D. Schubert, and G. K. Walker, 2005: Global changes of the water cycle intensity. *Journal of Climate*, **18**, 1591–1608.

Chadwick, R., P. Good, and K. Willett, 2016: A simple moisture advection model of specific humidity change over land in response to SST warming. *J. Climate*, **29**, 7613–7632,

Chahine, M. T., 1992: The hydrological cycle and its influence on climate. *Nature*, **359**, 373–380.

Chen, M., and Coauthors, 2008: Assessing objective techniques for gauge-based analyses of global daily precipitation, *J. Geophys. Res.*, **113**, D04110.

Collins, M., and Co-authors, 2013: Long-term Climate Change: Projections, Commitments and Irreversibility. In: *Climate Change 2013: The Physical Science Basis. Contribution of Working Group I to the Fifth Assessment Report of the Intergovernmental Panel on Climate Change* [Stocker, T.F., D. Qin, G.-K. Plattner, M. Tignor, S.K. Allen, J. Boschung, A. Nauels, Y. Xia, V. Bex and P.M. Midgley (eds.)]. Cambridge University Press, Cambridge, United Kingdom and New York, NY, USA

Cook, B. I., and R. Seager, 2013: The response of the North American monsoon to increased greenhouse gas forcing. *J. Geophys. Res. Atmos.*, **118**, 1690–1699.

CSIRO and Bureau of Meteorology, 2015: *Climate Change in Australia Information for Australia's Natural Resource Management Regions: Technical Report*. Australia: CSIRO and Bureau of Meteorology.

Daly, C., M. Halbleib, J. I. Smith, W. P. Gibson, M. K. Doggett, G. H. Taylor, J. Curtis, and P. P. Pasteris, 2008: Physiographically sensitive mapping of climatological temperature and precipitation across the conterminous United States. *International Journal of Climatology: a Journal of the Royal Meteorological Society*, **28**, 2031–2064.

Dettinger, M., 2011: Climate change, atmospheric rivers, and floods in California–a multimodel analysis of storm frequency and magnitude changes 1. *JAWRA Journal of the American Water Resources Association*, **47**, 514–523.

Easterling, D. R., and Coauthors, 2017: Precipitation change in the United States. In: *Climate Science Special Report: Fourth National Climate Assessment, Volume I* [Wuebbles, D.J., D.W. Fahey, K.A. Hibbard, D.J. Dokken, B.C. Stewart, and T.K. Maycock (eds.)]. U.S. Global Change Research Program, Washington, DC, USA.

Espinoza, V., D. E. Waliser, B. Guan, D. A. Lavers, and F. M. Ralph, 2018: Global analysis of climate change projection effects on atmospheric rivers. *Geophysical Research Letters*, **45**, 4299–4308.

Eyring, V., Bony, S., Meehl, G. A., Senior, C. A., Stevens, B., Stouffer, R. J., and Taylor, K. E.: Overview of the Coupled Model Intercomparison Project Phase 6 (CMIP6) experimental design and organization, *Geosci. Model Dev*., **9**, 1937-1958

Feng, Z., L. R. Leung, S. Hagos, R. A. Houze, C. D. Burleyson, and K. Balaguru, 2016: More frequent intense and long-lived storms dominate the springtime trend in central US rainfall. *Nature communications*, **7**, 1–8.

Gao, Y., J. Lu, L. R. Leung, Q. Yang, S. Hagos, and Y. Qian, 2015: Dynamical and thermodynamical modulations on future changes of landfalling atmospheric rivers over western North America. *Geophysical Research Letters*, **42**, 7179–7186.

Gershunov, A., T. Shulgina, F. M. Ralph, D. A. Lavers, and J. J. Rutz, 2017: Assessing the climate-scale variability of atmospheric rivers affecting western North America. *Geophysical Research Letters*, **44**, 7900–7908.

Guan, B., N. P. Molotch, D. E. Waliser, E. J. Fetzer, and P. J. Neiman, 2010: Extreme snowfall events linked to atmospheric rivers and surface air temperature via satellite measurements. *Geophysical Research Letters*, **37**.

Harris, I., T. J. Osborn, P. Jones, and D. Lister, 2020: Version 4 of the CRU TS monthly high-resolution gridded multivariate climate dataset *Sci. Data*, **7**, 109.

Held, I. M., and B. J. Soden, 2006: Robust responses of the hydrological cycle to global warming. *Journal of climate*, **19**, 5686–5699.

Hersbach, H., and Coauthors, 2020: The ERA5 global reanalysis. *Quarterly Journal of the Royal Meteorological Society*, **146**, 1999–2049.

Huntington, T. G., 2006: Evidence for intensification of the global water cycle: Review and synthesis. *Journal of Hydrology*, **319**, 83–95.

IPCC 2013: *Climate Change 2013: The Physical Science Basis. Contribution of Working Group I to the Fifth Assessment Report of the Intergovernmental Panel on Climate Change*. Cambridge University Press, Cambridge, UK and New York, NY.

Jin, C., B. Wang, and J. Liu, 2020: Future changes and controlling factors of the eight regional monsoons projected by CMIP6 models. *J. Climate*, **33**, 9307–9326.

Korzoun, V. I., Ed., 1974: *World Water Balance and Water Resources of the Earth*. Hydrometeoizdat, 638 pp.

Krishnan, R., J. Sanjay, C. Gnanaseelan, M. Mujumdar, A. Kulkarni, and S. Chakraborty, 2020: *Assessment of climate change over the Indian region: a report of the ministry of earth sciences (MOES), government of India*. Springer Nature.

Kundzewicz, Z. W., 2008: Climate change impacts on the hydrological cycle. *Ecohydrology & Hydrobiology*, **8**, 195–203.

Massoud, E., M. Turmon, J. Reager, J. Hobbs, Z. Liu, and C. H. David, 2020a: Cascading dynamics of the hydrologic cycle in California explored through observations and model simulations. *Geosciences*, **10**, 71.

Massoud, E. C., H. Lee, P. B. Gibson, P. Loikith, and D. E. Waliser, 2020b: Bayesian model averaging of climate model projections constrained by precipitation observations over the contiguous United States. *Journal of Hydrometeorology*, **21**, 2401–2418.

McKinnon, K. A., and C. Deser, 2021: The inherent uncertainty of precipitation variability, trends, and extremes due to internal variability, with implications for western U.S. water resources. *Journal of Climate*, **34**, 9605-9622.

Murphy, J. M., and Coauthors, 2018: *UKCP18 Land Projections: Science Report*. Exeter, UK: Met Office Hadley Centre. https://www.metoffice.gov.uk/pub/data/weather/uk/ukcp18/science-reports/UKCP18-Land-report.pdf.

Nace, R. L., 1969: World water inventory and control. *Water, Earth, and Man*, R. J. Chorley, Ed., Methuen, 31–42.

O'Neill, B. C., and Coauthors, 2016: The Scenario Model Intercomparison Project (ScenarioMIP) for CMIP6. *Geosci. Model Dev.*, **9**, 3461–3482.

Oki, T., and S. Kanae, 2006: Global hydrological cycles and world water resources. *science*, **313**, 1068–1072.

——, D. Entekhabi, and T. I. Harrold, 1999: The global water cycle. *Global energy and water cycles*, **10**, 27.

Pascolini-Campbell, M., J. T. Reager, H. A. Chandanpurkar, and M. Rodell, 2021: A 10 per cent increase in global land evapotranspiration from 2003 to 2019. *Nature*, **593**, 543-547.

Rodell, M., and Coauthors, 2015: The observed state of the water cycle in the early twenty-first century. *Journal of Climate*, **28**, 8289–8318.

Ruiz-Barradas, A., and S. Nigam, 2005: Warm season rainfall variability over the US Great Plains in observations, NCEP and ERA-40 reanalyses, and NCAR and NASA atmospheric model simulations. *Journal of Climate*, **18**, 1808–1830.

——, and ——, 2006: IPCC's twentieth-century climate simulations: Varied representations of North American hydroclimate variability. *Journal of climate*, **19**, 4041–4058.

Ryu, J., and K. Hayhoe, 2014: Understanding the sources of Caribbean precipitation biases in CMIP3 and CMIP5 simulations. *Climate Dyn*., **42**, 3233–3252.

Schneider, U., Becker, A., Finger, P., Meyer-Christoffer, A. and Ziese, M., 2018: GPCC Full Data Monthly Product Version 2018 at 0.25°: Monthly land-surface precipitation from rain gauges built on GTS-based and historical data; doi:10.5676/DWD_GPCC/FD_M_V2018_025.

Schubert, S. D., M. J. Suarez, P. J. Pegion, R. D. Koster, and J. T. Bacmeister, 2004: Causes of long-term drought in the US Great Plains. *Journal of Climate*, **17**, 485–503.

Tabari, H., P. Hosseinzadehtalaei, W. Thiery, and P. Willems, 2021: Amplified drought and flood risk under future socioeconomic and climatic change. *Earth's Future*, **9**, e2021EF002295.

Trenberth, K. E., and C. J. Guillemot, 1996: Physical processes involved in the 1988 drought and 1993 floods in North America. *Journal of Climate,* **9**, 1288–1298.

——, L. Smith, T. Qian, A. Dai, and J. Fasullo, 2007: Estimates of the global water budget and its annual cycle using observational and model data. *Journal of Hydrometeorology*, **8**, 758–769.

USGCRP, 2017: *Climate Science Special Report: Fourth National Climate Assessment (NCA4).* Vol. I, D. J. Wuebbles et al., Eds., U.S Global Research Program, 470 pp., http://doi.org/10.7930/J0J964J6.

Vecchi, G. A., and B. J. Soden, 2007: Global warming and the weakening of the tropical circulation. *J. Climate*, **20**, 4316– 4340.

Waliser, D., K.-W. Seo, S. Schubert, and E. Njoku, 2007: Global water cycle agreement in the climate models assessed in the IPCC AR4. *Geophysical research letters*, **34**.

Walsh, J., and Coauthors, 2014: Ch. 2: Our changing climate. *Climate Change Impacts in the United States: The Third National Climate Assessment*. Melillo, J.M., T.C. Richmond, and G.W. Yohe, Eds. U.S. Global Change Research Program, Washington, D.C., 19-67.

Wang, B., C. Jin, and J. Liu, 2020: Understanding future change of global monsoons projected by CMIP6 models. *J. Climate*, **33**, 6471–6489.

Wang, H., R. Fu, A. Kumar, and W. H. Li, 2010: Intensification of summer rainfall variability in the southeastern United States during recent decades. *J. Hydrometeor.*,**11**, 1007–1018.

Warner, M. D., C. F. Mass, and E. P. Salathe Jr, 2015: Changes in winter atmospheric rivers along the North American west coast in CMIP5 climate models. *Journal of Hydrometeorology*, **16**, 118–128.

Watterson, I. G., R. J. Keane, M. Dix, T. Ziehn, T. Andrews, and Y. Tang, 2021: Analysis of CMIP6 atmospheric moisture fluxes and the implications for projections of future change in mean and heavy rainfall. *International Journal of Climatology*, **41**, E1417–E1434.

Xie, P., M. Chen, S. Yang, A. Yatagai, T. Hayasaka, Y. Fukushima, and C. Liu, 2007: A gauge-based analysis of daily precipitation over East Asia. *Journal of Hydrometeorology*, **8**, 607–626.

Zhou, W., L. R. Leung, F. Song, and J. Lu, 2020: Future changes in the Great Plains Low-Level Jet governed by seasonally dependent pattern changes in the North Atlantic Subtropical High. *Geophysical Research Letters*, **48**, e2020GL090356.

Fig. 1

Click here to access/download
**Non-Rendered Figure**
figure01.pdf

Fig. 2

Click here to access/download
**Non-Rendered Figure**
figure02.pdf

Fig. 3

Click here to access/download
**Non-Rendered Figure**
figure03.pdf

Fig. 4

Click here to access/download
**Non-Rendered Figure**
figure04.pdf

Fig. 5

Click here to access/download
**Non-Rendered Figure**
figure05.pdf

Fig. 6

Click here to access/download
**Non-Rendered Figure**
figure06.pdf

Fig. 7

Click here to access/download
**Non-Rendered Figure**
figure07.pdf

Fig. 8

Click here to access/download
**Non-Rendered Figure**
figure08.pdf

Fig. 9

Click here to access/download
**Non-Rendered Figure**
figure09.pdf

Fig. 10

Click here to access/download

**Non-Rendered Figure**

figure10.pdf

Fig. 11

Click here to access/download

**Non-Rendered Figure**

figure11.pdf

Fig. 12

Click here to access/download
**Non-Rendered Figure**
figure12.pdf

Fig. 13

Click here to access/download
**Non-Rendered Figure**
figure13.pdf

Fig. 14

Click here to access/download
**Non-Rendered Figure**
figure14.pdf